

COBIPULSE: A Systematic Search for Compact Binary Millisecond Pulsars

MARCO TURCHETTA,¹ MANUEL LINARES,^{1,2} KARRI KOLJONEN,¹ JORGE CASARES,^{3,4} PAULO A. MILES-PÁEZ,⁵
PABLO RODRÍGUEZ-GIL,^{3,4} TARIQ SHAHBAZ,^{3,4} AND JORDAN A. SIMPSON¹

¹*Department of Physics, Norwegian University of Science and Technology, NO-7491 Trondheim, Norway*

²*Departament de Física, EEBE, Universitat Politècnica de Catalunya, Av. Eduard Maristany 16, E-08019 Barcelona, Spain*

³*Instituto de Astrofísica de Canarias, E-38205 La Laguna, Tenerife, Spain*

⁴*Departamento de Astrofísica, Universidad de La Laguna, E-38206 La Laguna, Tenerife, Spain*

⁵*Centro de Astrobiología, CSIC-INTA, Camino Bajo del Castillo s/n, 28692 Villanueva de la Cañada, Madrid, Spain*

ABSTRACT

We report here the results obtained from a systematic optical photometric survey aimed at finding new compact binary millisecond pulsars (also known as “spiders”): the COmpact BInary PULsar SEarch (COBIPULSE). We acquired multi-band optical images over one year around 33 unidentified *Fermi*-LAT sources, selected as pulsar candidates based on their curved GeV spectra and steady γ -ray emission. We present the discovery of four optical variables coinciding with the *Fermi* sources 3FGL J0737.2–3233, 3FGL J2117.6+3725 (two systems in this field) and 3FGL J2221.6+6507, which we propose as new candidate spider systems. Indeed, they all show optical flux modulation consistent with orbital periods of 0.3548(5) d, 0.25328(6) d, 0.441961(2) d, and 0.165(4) d, respectively, with amplitudes $\gtrsim 0.3$ mag and colors compatible with companion star temperatures of 5000–6000 K. These properties are consistent with the “redback” sub-class of spider pulsars. If confirmed as a millisecond pulsar, 3FGL J0737.2–3233 will be the closest known spider to Earth ($D = 659^{+16}_{-20}$ pc, from *Gaia*-DR3 parallax). We searched and did not find any X-ray sources matching our four candidates, placing 3σ upper limits of $\sim 10^{31}$ – 10^{32} erg s^{−1} (0.3–10 keV) on their soft X-ray luminosities. We also present and discuss other multi-wavelength information on our spider candidates, from infrared to X-rays.

Keywords: High energy astrophysics (739) — Close binary stars (254) — Millisecond pulsars (1062)
— Variable stars (1761)

1. INTRODUCTION

Millisecond pulsars (MSPs) are “recycled” neutron stars with spin periods $\simeq 1$ –30 ms, which they reach after a Gyr-long phase of accretion from a low-mass companion star (Radhakrishnan & Srinivasan 1982; Bhattacharya & van den Heuvel 1991). This low-mass X-ray binary (LMXB) stage persists until the mass transfer rate decreases and allows the activation of a radio MSP, powered by its rotational energy (Tauris et al. 2013).

About 20% of the currently known radio MSPs are found in compact binary systems (according to the ATNF Pulsar Catalog¹), with orbital periods $\lesssim 1$ d. Given such tight orbits, the wind of relativistic particles powered by the loss of rotational energy of the pulsar can strongly irradiate and strip matter off the companion star. This gives a proposed formation chan-

nel for isolated MSPs, if the pulsar has enough time to fully consume its companion (van den Heuvel & van Paradijs 1988). Such destructive effect also inspired cannibalistic arachnid nicknames for these systems: *redback* (RB) and *black widow* (BW) MSPs, with low-mass non-degenerate companions ($M_2 \simeq 0.3$ – $0.7 M_\odot$) and very low-mass semi-degenerate companions ($M_2 \sim 0.01 M_\odot$) for RBs and BWs, respectively (Fruchter et al. 1988; Roberts 2012). Both sub-types are collectively known as *spiders*.

The recycling scenario for MSP formation outlined above was confirmed by the discovery of accreting MSPs within LMXBs (Wijnands & van der Klis 1998), as well as three particular RBs known as transitional MSPs (Archibald et al. 2009; Papitto et al. 2013; Bassa et al. 2014). The latter change between the disk/LMXB and radio pulsar states on timescales of a few weeks, suggesting RBs to be the evolutionary link between these two phases. Generally, spiders provide a unique oppor-

¹ <https://www.atnf.csiro.au/research/pulsar/psrcat/>

tunity to probe the intrabinary shock between pulsar and companion winds (Wadiasingh et al. 2018), where charged particles emit synchrotron radiation which dominates the X-ray band (Gentile et al. 2014; Linares 2014). Furthermore, these systems represent promising environments to find massive neutron stars (Linares 2020), as they underwent a long phase of mass accretion to reach millisecond spin periods.

Until 2008, spiders were rarely detected in blind radio surveys² due to unknown orbital acceleration and eclipses of the pulsations occurring during a large fraction of the orbit. The radio pulses are absorbed and dispersed by the material stripped off the companion star (D’Amico et al. 2001). Since its launch in 2008, the *Fermi* Large Area Telescope (*Fermi*-LAT) has dramatically boosted the discovery of MSPs in general, and spiders in particular. The third *Fermi*-LAT pulsar catalog reports at least 119 new MSPs, detected either as γ -ray or radio MSPs via radio searches targeting unidentified *Fermi*-LAT sources (Smith et al. 2023). Among these, 57 spiders have been discovered in the Galactic field, while 17 more systems with no detected pulsations have been classified as spider candidates based on their optical light curve shape and multi-wavelength phenomenology (Nedreaas 2024).

Spiders can also be discovered through their variable optical counterparts, dominated by the companion flux and showing orbital modulation (e.g. Linares et al. 2017; Swihart et al. 2021; Au et al. 2023). Optical light curves of all currently known BWs exhibit a single bright maximum per orbit with sharp minima and ≈ 1 mag-large peak-to-peak amplitudes, due to the pulsar irradiating flux overwhelming the intrinsic emission of the cold companion, with typical base temperatures of $T_b \simeq 1000$ –3000 K. RB companions, on the other hand, are more massive and hotter than BW companions, with $T_b \simeq 4000$ –6000 K. About half of the known RBs show little or no signs of irradiation and ellipsoidal modulation produced by the visibility of the tidally distorted companion star, with sinusoidal optical light curves showing two maxima per orbit (Turchetta et al. 2023). Such systems exhibit smaller peak-to-peak amplitudes $\simeq 0.3$ mag with respect to spiders in the irradiation regime (Dodge et al. 2024).

Despite ongoing efforts, the latest *Fermi*-LAT catalog (4FGL-DR4, Ballet et al. 2023) lists more than 2100 unassociated sources. Many of these might be spiders still “hidden” in our Galaxy: based on population synthesis models (Gonthier et al. 2018) we predict the de-

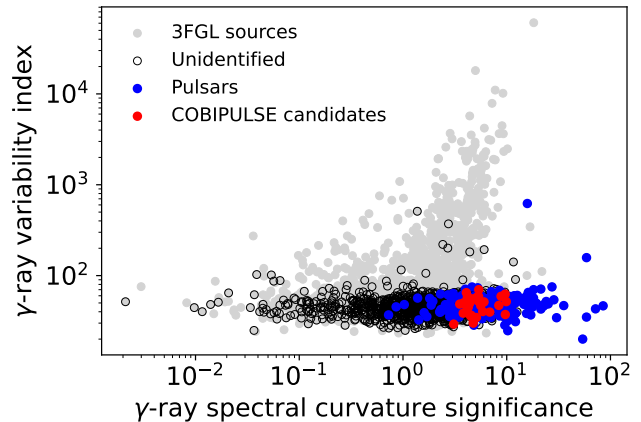


Figure 1. γ -ray variability versus γ -ray curvature significance plot, where all *Fermi*-LAT 3FGL sources are shown as gray filled circles, unidentified objects as black empty circles, identified pulsars as blue filled circles, and COBIPULSE candidates as red filled circles.

tection of at least ≈ 70 new MSPs in the next five years. In this context, searching for spiders through optical observations of unassociated *Fermi*-LAT sources constitutes a promising strategy. Indeed, there are many cases of spiders detected as MSPs only years after the discovery of their optical variable counterpart, by pointing radio facilities towards their precise sky location (see e.g. Romani 2015 and Clark et al. 2021 for PSR J2039–5617, Linares et al. 2017 and Perez et al. 2023 for PSR J0212+5321, Au et al. 2023 and Dodge et al. 2024 for PSR J1910–5320).

In this paper we present the COmpact BInary PULsar SEarch (COBIPULSE), a systematic optical photometric survey targeting 33 unidentified γ -ray sources selected as promising pulsar candidates from the *Fermi*-LAT 3FGL catalog (Acero et al. 2015). In Section 2 we describe our selection criteria for the *Fermi* fields of view, data acquisition, and how we performed photometry and periodicity searches for every source detected in the field. In Section 3 we report the results of our survey, with periodograms and folded light curves of the optical variables classified as spider candidates. In Section 4 we discuss separately each discovered candidate and search for radio, IR and X-ray counterparts to our optical candidates from known catalogs. We summarize our main findings in Section 5.

2. OBSERVATIONS AND DATA ANALYSIS

2.1. Pulsar candidates from the *Fermi*-3FGL catalog

We built our sample of candidates for COBIPULSE based on the two main properties shown by pulsars in the γ -ray *Fermi*-LAT energy band: they are steady γ -ray emitters with curved spectra in the 0.1–300 GeV en-

² <https://www.astro.umd.edu/~eferrara/pulsars/GalacticMSPs.txt>

Table 1. Log of COBIPULSE observations.

Field 3FGL source	Telescope (diameter)	Instrument (configuration)	Date (evening)	Time (UT)	Images in g' (nr \times exp. time)	Images in r' (nr \times exp. time)	Images in i' (nr \times exp. time)
J0238.0+5237	STELLA-1.2m	WiFSIP-1x1	2015-09-04	01:22–04:57	9 \times 300 s	18 \times 300 s	9 \times 300 s
J0312.1–0921	STELLA-1.2m	WiFSIP-1x1	2015-11-14	00:01–03:33	7 \times 300 s	17 \times 300 s	7 \times 300 s
J0318.1+0252	STELLA-1.2m	WiFSIP-1x1	2015-11-11	21:36–23:32	4 \times 300 s	9 \times 300 s	4 \times 300 s
J0336.1+7500	STELLA-1.2m	WiFSIP-1x1	2015-11-07	21:12–23:09	6 \times 300 s	12 \times 300 s	5 \times 300 s
			2015-11-25	20:18–23:56	6 \times 300 s	11 \times 300 s	8 \times 300 s
J0545.6+6019	STELLA-1.2m	WiFSIP-1x1	2015-09-17	02:11–05:46	9 \times 300 s	18 \times 300 s	9 \times 300 s
J0758.6–1451	STELLA-1.2m	WiFSIP-1x1	2015-11-28	01:56–05:33	9 \times 300 s	18 \times 300 s	9 \times 300 s
			2016-01-16	00:44–04:17	8 \times 300 s	17 \times 300 s	8 \times 300 s
J0953.7–1510	STELLA-1.2m	WiFSIP-1x1	2015-12-19	02:37–04:07	4 \times 300 s	9 \times 300 s	4 \times 300 s
			2016-01-20	03:13–04:17	4 \times 300 s	7 \times 300 s	3 \times 300 s
J1120.6+0713	STELLA-1.2m	WiFSIP-1x1	2015-12-21	02:47–06:25	9 \times 300 s	18 \times 300 s	8 \times 300 s
			2016-01-22	00:43–04:23	9 \times 300 s	18 \times 300 s	9 \times 300 s
J1543.5–0244	STELLA-1.2m	WiFSIP-1x1	2016-03-01	02:49–06:30	8 \times 300 s	17 \times 300 s	8 \times 300 s
			2016-03-17	03:04–05:29	4 \times 300 s	7 \times 300 s	8 \times 300 s
			2016-04-01	01:46–05:31	8 \times 300 s	18 \times 300 s	9 \times 300 s
J1601.9+2306	STELLA-1.2m	WiFSIP-1x1	2015-08-26	21:04–00:39	9 \times 300 s	18 \times 300 s	9 \times 300 s
			2016-02-18	02:59–04:31	5 \times 300 s	10 \times 300 s	4 \times 300 s
			2016-03-06	02:11–03:18	4 \times 300 s	7 \times 300 s	3 \times 300 s
J1625.1–0021	STELLA-1.2m	WiFSIP-1x1	2016-03-29	02:05–05:49	9 \times 300 s	16 \times 300 s	9 \times 300 s
			2016-04-19	00:08–03:53	9 \times 300 s	18 \times 300 s	9 \times 300 s
J1730.6–0357	STELLA-1.2m	WiFSIP-1x1	2016-04-10	02:00–05:44	8 \times 300 s	18 \times 300 s	9 \times 300 s
			2016-04-26	01:22–05:02	9 \times 300 s	18 \times 300 s	9 \times 300 s
J2103.7–1113	STELLA-1.2m	WiFSIP-1x1	2015-11-14	21:23–22:50	4 \times 300 s	8 \times 300 s	3 \times 300 s
J2212.5+0703	STELLA-1.2m	WiFSIP-1x1	2015-08-06	01:16–02:20	4 \times 300 s	6 \times 300 s	3 \times 300 s
			2015-08-12	00:36–04:11	9 \times 300 s	17 \times 300 s	9 \times 300 s
J2221.6+6507	STELLA-1.2m	WiFSIP-1x1	2015-11-01	21:31–01:02	9 \times 300 s	18 \times 300 s	9 \times 300 s
			2015-11-17	20:37–00:10	9 \times 300 s	18 \times 300 s	9 \times 300 s
J2233.1+6542	STELLA-1.2m	WiFSIP-1x1	2015-09-05	01:48–05:24	9 \times 300 s	18 \times 300 s	9 \times 300 s
J2310.1–0557	STELLA-1.2m	WiFSIP-1x1	2015-10-11	02:22–03:51	4 \times 300 s	9 \times 300 s	4 \times 300 s
			2015-11-10	21:39–00:26	7 \times 300 s	12 \times 300 s	6 \times 300 s
J1225.9+2953	INT-2.5m	WFC-1x1	2015-06-05	23:07–00:35	12 \times 60 s	24 \times 60 s	12 \times 60 s
J1630.2–1052	INT-2.5m	WFC-1x1	2015-06-03	01:00–02:42	7 \times 180 s	14 \times 180 s	7 \times 180 s
J1827.7+1141	INT-2.5m	WFC-1x1	2015-06-03	03:00–04:51	12 \times 180 s	22 \times 180 s	12 \times 180 s
J1829.2+3229	INT-2.5m	WFC-1x1	2015-06-04	00:41–02:32	12 \times 60 s	29 \times 60 s	15 \times 60 s
J1950.2+1215	INT-2.5m	WFC-1x1	2015-06-05	03:31–04:36	9 \times 60 s	18 \times 60 s	9 \times 60 s
J2117.6+3725	INT-2.5m	WFC-1x1	2015-06-04	02:58–05:20	19 \times 60 s	38 \times 60 s	19 \times 60 s
J0514.6–4406	LCO-1m	Sinistro-1x1	2015-11-02	05:11–08:31	9 \times 300 s	18 \times 300 s	9 \times 300 s
			2015-11-04	04:00–07:20	9 \times 300 s	18 \times 300 s	8 \times 300 s
			2015-11-05	05:12–08:32	9 \times 300 s	18 \times 300 s	9 \times 300 s
			2015-11-06	05:09–05:43	3 \times 300 s	5 \times 300 s	2 \times 300 s
			2015-11-07	04:50–08:10	9 \times 300 s	18 \times 300 s	9 \times 300 s
			2015-11-20	04:25–07:45	9 \times 300 s	18 \times 300 s	8 \times 300 s
J0737.2–3233	LCO-1m	Sinistro-1x1	2015-11-09	05:14–08:34	9 \times 300 s	18 \times 300 s	9 \times 300 s
			2015-11-12	05:09–08:29	9 \times 300 s	18 \times 300 s	9 \times 300 s
			2015-11-21	03:47–07:07	9 \times 300 s	18 \times 300 s	9 \times 300 s
J0933.9–6232	LCO-1m	Sinistro-1x1	2015-12-04	04:53–08:13	9 \times 300 s	17 \times 300 s	9 \times 300 s
			2015-12-08	04:55–06:43	6 \times 300 s	11 \times 300 s	5 \times 300 s
			2015-12-26	03:51–06:47	8 \times 300 s	18 \times 300 s	9 \times 300 s
J1035.7–6720	LCO-1m	Sinistro-1x1	2015-12-19	05:06–08:26	9 \times 300 s	18 \times 300 s	9 \times 300 s
			2015-12-23	04:39–07:36	9 \times 300 s	18 \times 300 s	8 \times 300 s
			2015-12-27	04:50–08:10	8 \times 300 s	17 \times 300 s	8 \times 300 s
J1119.9–2204	LCO-1m	Sinistro-1x1	2016-01-08	03:45–06:41	9 \times 300 s	18 \times 300 s	8 \times 300 s
			2016-02-19	02:01–05:21	9 \times 300 s	18 \times 300 s	9 \times 300 s
J1231.6–5113	LCO-1m	Sinistro-1x1	2016-03-28	23:54–02:50	9 \times 300 s	17 \times 300 s	8 \times 300 s
			2016-02-19	06:00–09:20	9 \times 300 s	18 \times 300 s	9 \times 300 s
J1744.1–7619	LCO-0.4m	SBIG-2x2	2016-02-21	04:09–07:29	9 \times 300 s	18 \times 300 s	9 \times 300 s
			2016-06-13	09:46–12:09	11 \times 150 s	17 \times 150 s	12 \times 150 s
J1757.7–6030	LCO-0.4m	SBIG-2x2	2016-06-12	10:24–12:35	11 \times 150 s	19 \times 150 s	11 \times 150 s
J1946.4–5403	LCO-0.4m	SBIG-2x2	2016-06-07	12:18–13:50	2 \times 150 s	3 \times 150 s	1 \times 150 s
			2016-06-12	16:13–19:41	8 \times 150 s	8 \times 150 s	4 \times 150 s
J2039.9–5618	LCO-0.4m	SBIG-2x2	2016-07-28	14:31–17:57	17 \times 150 s	34 \times 150 s	17 \times 150 s
			2016-08-06	11:38–14:58	13 \times 150 s	24 \times 150 s	12 \times 150 s

ergy range (Ackermann et al. 2012). These were quantified in the 3FGL catalog by the variability index and the spectral curvature significance, respectively (for details see Eqs. (3) and (4) in Nolan et al. 2012). We therefore selected, among the 1010 3FGL unidentified sources available in 2015, pulsar candidates that fulfilled all the following criteria³:

1. They have spectral curvature significance higher than 3σ .
2. Their variability index is lower than 100.
3. They are located at Galactic latitudes $|b| > 5^\circ$ (to avoid contamination from the diffuse γ -ray emission close to the Galactic plane).
4. The semi-major axis of the *Fermi* 95% error ellipse is $< 30'$ (to fit them in the STELLA, INT and LCO fields of view; see Section 2.2).

This led us to the 33 COBIPULSE candidates selected for this study, listed in Table 1. As we can see from Figure 1, COBIPULSE candidates (shown as red circles) are all located in the bottom right region of the γ -ray variability-curvature diagram, along with the majority of the known pulsar population (reported in blue).

2.2. Observations and optical photometry

We acquired optical images of the 33 selected fields with the 1.2-m STELLA, 2.5-m INT, 1-m LCO, and 0.4-m LCO telescopes, using the WiFSIP, WFC, Sinistro, and SBIG cameras mounted on each of them, respectively. The observations were taken over 14 months, from 2015 June 3 to 2016 August 6, alternating the SDSS g' , r' and i' optical filters across the nights. We chose to cycle the exposures through the sequence g' - r' - i' - r' to improve the sampling in r' and investigate the source variability in this band, while obtaining color information from g' and i' . We report in Table 1 details of the instrumental setups used for our observations.

We processed STELLA/WiFSIP, LCO/Sinistro, and LCO/SBIG data using their respective data-processing pipelines, which included tasks such as bad-pixel masking, bias subtraction and flat-field correction (see Brown et al. 2013, Weber et al. 2016, and McCully et al. 2018 for more details). Concerning the INT data, we performed data reduction separately for each of the four CCDs in the WFC mosaic camera using standard

routines in IRAF⁴. For INT/WFC, we performed our search only with CCD n.4 data, which contains the entire 95% error ellipse for each of the 6 *Fermi*-3FGL fields observed with this telescope.

We combined the images acquired from a given field into a single median image for each of the optical bands, g' , r' and i' , to obtain a deeper source detection sensitivity (see the r' -band fields in Appendix A, Figures A1-A7). We identified all the sources in the field having a signal-to-noise ratio ≥ 2 in the combined frames using the SEP⁵ package (Barbary et al. 2016), based on the SExtractor software (Bertin & Arnouts 1996). Using this detection threshold, our survey is sensitive down to magnitudes $r' \simeq 19, 21, 21$ and 22 for 0.4-m LCO, 1-m LCO, 1.2-m STELLA, and 2.5-m INT, respectively. This allows us to detect potential red-back systems, which typically cover the magnitude range $r' \simeq 14$ – 20 . However, we stress that the faintest sources identified in the median images might be lost or barely detected in some of the individual frames, affecting the extraction of their optical light curves. We detected between about 200 and 22000 sources, depending on each field and band (Table 2).

Next, we performed circular aperture photometry systematically using SEP on all the identified stars. We experimented with different aperture radii, and concluded that $1.2\times$ the average full-width at half maximum (FWHM) is optimal to minimize sky noise contribution and photometry contamination between nearby stars in the most crowded fields. We used three different sets of comparison stars (one for each optical filter g' , r' and i'), selected as the most stable sources in the field using the ASTROSOURCE⁶ package (Fitzgerald et al. 2021), all showing variability with rms amplitudes of $\simeq 0.001$ – 0.01 mag⁷. We also restricted the selection of comparison stars to sources in the magnitude range $\simeq 14$ – 16 , with brightness similar to or greater than our targets of interest (the brightest known spider PSR J0212+5321 has $r' \simeq 14.3$, Linares et al. 2017), and far from the saturation regime of the detectors.

⁴ <https://iraf-community.github.io/>

⁵ <https://github.com/kbarbary/sep>

⁶ <https://github.com/zemogle/astrosource>

⁷ By summing together the counts measured from N reference stars, we improve the signal-to-noise ratio on the apparent magnitudes of our targets by a factor of \sqrt{N} (Honeycutt 1992).

³ The selection and optical observations of these *Fermi* fields were performed in 2015, thus we used the 3FGL catalog (Acero et al. 2015) back then instead of the latest 4FGL-DR4 (Ballet et al. 2023).

2.3. Variable selection and periodicity search

We computed the average differential magnitude Δm ⁸ and its standard deviation σ for each source detected in the r' -band, where the data sampling is best (twice the g' and i' -band cadence, Sec. 2.2). The corresponding σ - Δm plots are shown in Appendix B (Figures B1-B6). For each COBIPULSE field we considered all the sources fulfilling the criteria described below for further study:

1. They lie inside a square centered on the *Fermi*-3FGL coordinates, with sides twice the semi-major axis of the 95% error ellipse.
2. Their magnitude standard deviation σ is larger than the median value of σ computed over the sources lying in the same differential magnitude bin Δm of width 0.1 mag. Since sources showing peak-to-peak amplitudes ≥ 0.1 mag typically corresponded to $\sigma \geq 2\times$ the median, we chose $1\times$ the median as a conservative σ -threshold to not miss any variable. When we have less than 5 sources detected in the corresponding differential magnitude bin, we skip this filtering step and use only criterion n.1, as the statistics are too poor to establish whether a source is variable or not.

The numbers for these sources of interest are reported in the 5th column of Table 2, labeled as “photometric variables”. We detected between 30 and 1700 photometric variables per field.

We then performed Lomb-Scargle (LS; Lomb 1976; Scargle 1982) and phase-dispersion minimization periodicity searches (PDM; Stellingwerf 1978) systematically on the r' -band light curve of each source selected in the above step. The inspected grid of periods spans the range 0.02–2.5 d, to accommodate typical spider orbital periods (see Table 1 in Linares & Kachelrieß 2021), using a period resolution of $\simeq 2$ min. For each case, we folded the r' -band light curves on the periods corresponding to the maximum and minimum of the LS and PDM periodograms, respectively. After checking for possible spurious variability introduced by stars close to the target, we considered all the sources showing sinusoid-like folded light curves, sharp flux minima⁹ or monotonically varying light curves in the r' -band. Also, the g' and i' -band light curves have been folded with the best photometric period P_{best} , that we chose from the method

(LS or PDM) yielding the smoothest light curve shape. We classified as “smooth variables” all the sources investigated above showing the same trend consistently in their g' , r' and i' -band light curves, finding between 0 and 5 smooth variables per field (numbers reported in the 6th column of Table 2). The latter selection step excludes undesired variables from our search, like spurious/artificial variables, flares and planetary transits.

We evaluated the significance of the detected photometric periods by using a Fisher randomization test (Linnell Nemec & Nemec 1985). This method consists in permuting the original sequence of magnitudes m_i measured at the times t_i to assign them a different time t_j , computing then a new periodogram on this shuffled time series. We repeated such process for $N \sim 10000$ times for all our smooth variables. Then we considered the number of permutations whose LS/PDM periodogram contained a maximum/minimum which is larger/smaller than the power we found from the unrandomized dataset at any period. This represents the probability that no periodic component is present in the data, known as false-alarm-probability (FAP), with the detection confidence level corresponding to $1 - \text{FAP}$.

To estimate the uncertainty in the photometric periods, we generated mock light curves by introducing artificial Gaussian noise, where the magnitude m'_i at the i -th point was drawn from a Gaussian distribution with mean value m_i and standard deviation σ_{m_i} , with m_i and σ_{m_i} indicating the magnitude at the i -th point of the original light curve and its measurement error, respectively. We performed the same periodicity search as described above for the mock light curves and recorded the periods corresponding to the maximum/minimum values of their LS/PDM periodograms. We repeated such procedure for $N \sim 1000$ different variations of the original light curve, finding $P_{\text{best},i}$ for each one of them. We assumed the standard deviation $\sigma_{P_{\text{best}}}$ of $P_{\text{best},i}$ as the error on the photometric period estimated from the original data.

2.4. Supplementary data from the ZTF optical survey

To expand the light curves of the northern sky sources we deemed as “smooth variables” in the previous section, we used the Zwicky Transient Facility (ZTF) survey data from the latest public release (2018 March–2023 November, Bellm et al. 2019). For 13 of our fields which are covered by ZTF (declination $\delta > -31^\circ$), we downloaded data for the g' and r' bands from the IRSA light curve service¹⁰, extracted using circular apertures

⁸ The differential magnitude is defined as the difference between the apparent magnitudes of target and comparison stars, determined from the ratio of target to comparison measured counts.

⁹ Optical light curves of spiders typically have a sinusoidal shape in the ellipsoidal regime and sharp minima with larger amplitudes in the irradiated regime (see Section 1).

¹⁰ https://irsa.ipac.caltech.edu/docs/program_interface/ztf_lightcurve.api.html

of radius $0.5 \times \text{FWHM}$ of their stellar point-spread function (PSF) (Bellm et al. 2019). Then, we applied the same periodicity search methods explained in Section 2.3.

The much longer time span of ZTF with respect to the COBIPULSE survey allowed us to confirm or refute as variables the northern sources showing monotonic variability or poor data sampling in our light curves. Furthermore, this analysis was useful to check and possibly increase the accuracy of the photometric periods when full phase coverage was missing in our data (see Section 3.2). Among the northern sources previously referred to as “smooth variables”, we thus classified “periodic variables” as those displaying a periodic pattern in the ZTF light curves consistent with the COBIPULSE light curves (numbers are reported in the 7th column of Table 2). Concerning the southern sky variable sources picked out in Section 2.3, we have been able to claim all of them as “periodic variables” based solely on our survey, as they were observed across multiple nights covering more than one orbit.

2.5. Classification of spider candidates

We use the following multi-wavelength scheme to classify a source as a potential spider candidate (numbers reported in the 8th column of Table 2):

1. *Unknown source*: It lacks a previous firm classification or published optical light curve.
2. *γ -rays*: It is located inside the corresponding *Fermi*-3FGL 95% error ellipse. An additional match with the latest 4FGL associated source would strengthen the spider identification.
3. *Optical*: Its multi-band optical light curves show a sinusoidal shape or sharp flux minima (see Section 2.3), with peak-to-peak amplitudes ≥ 0.1 mag. This threshold value takes into account also possible face-on inclinations.

Furthermore, we searched for matching X-ray sources in the *Chandra*, *Swift*, *XMM-Newton* and *eROSITA* latest catalogs (Evans et al. 2020; Evans et al. 2020; Webb et al. 2020; Merloni et al. 2024, respectively) using a search radius of $3''$ around the optical location. Detecting an X-ray source strengthens the spider association, as in these systems we usually observe X-ray emission produced by the intra-binary shock (see Section 1). However, the distance might be poorly constrained (see Section 4) and some of the known spiders are faint X-ray emitters ($L_X < 10^{31}$ erg s⁻¹). Together with the different depth of X-ray observations in different fields, this implies that the absence of an X-ray counterpart does not rule out the optical source as a spider candidate.

3. RESULTS

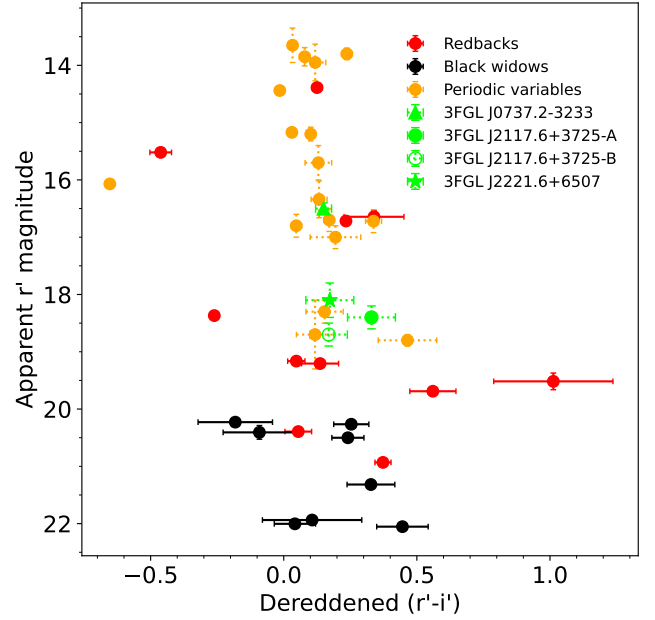


Figure 2. Apparent r' magnitude versus intrinsic (dereddened) $(r' - i')$ color. RBs and BWs are shown as red and black circles, respectively, with corresponding values taken from *Pan-STARRS* 1 catalog magnitudes. The periodic variables and spider candidates identified in this work are marked with orange circles and different green symbols for each system, respectively. For both variables and candidates we plot the average value computed from their light curves, with dotted lines indicating their magnitude range on the y -axis and the standard deviation of their color on the x -axis.

We report the main results obtained from our analysis in Table 2, for each *Fermi*-3FGL pulsar candidate. This wide-field optical survey led to the identification of 21 periodic variables in total, 3 of them newly discovered¹¹. By following the classification method outlined in Section 2.5, we identified 4 spider candidates in three different 3FGL fields: 3FGL J0737.2–3233, 3FGL J2117.6+3725-A, 3FGL J2117.6+3725-B and 3FGL J2221.6+6507 (see Sections 3.1, 3.2, and 3.3 for details). We summarize their main properties in Table 3. The corresponding periodograms and multi-band optical light curves are shown in the left and upper-right panels, respectively, of Figures 4, 6, 8, and 11. We report in Appendix C detailed information and optical light curves for all the other 17 periodic variables found

¹¹ We checked and did not find any variable star classification or optical light curve in the literature for these sources from *Catalina Sky Survey* (CSS; Drake et al. 2017), *ATLAS* (Heinze et al. 2018), *ZTF* (Chen et al. 2020), and *Gaia*-Data Release 3 (DR3; Gaia Collaboration 2023; Rimoldini et al. 2022) variables catalog.

Table 2. Photometry and periodicity search results.

Field 3FGL	Sources in g' (nr)	Sources in r' (nr)	Sources in i' (nr)	Phot. variables (nr)	Smooth variables (nr)	Per. variables (nr)	Spider candidates (nr)
STELLA/WiFSIP (1.2m)							
J0238.0+5237	4081	5997	6245	204	1	1	–
J0312.1–0921	351	564	479	44	–	–	–
J0318.1+0252	302	220	177	36	3	–	–
J0336.1+7500	2600	2576	2862	80	–	–	–
J0545.6+6019	2189	3100	3563	83	–	–	–
J0758.6–1451	2399	3702	3167	1293	3	3	–
J0953.7–1510	1011	1445	1180	93	1	1	–
J1120.6+0713	386	513	536	43	–	–	–
J1543.5–0244	1550	1141	1585	322	1	1	–
J1601.9+2306	979	778	628	150	–	–	–
J1625.1–0021	626	820	446	33	–	–	–
J1730.6–0357	5266	7499	6432	450	1	–	–
J2103.7–1113	609	930	1397	70	–	–	–
J2212.5+0703	1956	3828	3011	175	1	1	–
J2221.6+6507	3802	6210	6050	1169	3	3	1
J2233.1+6542	900	1755	3123	202	1	1	–
J2310.1–0557	704	790	1402	189	1	–	–
INT/WFC (2.5-m)							
J1225.9+2953	715	752	513	56	–	–	–
J1630.2–1052	1430	2186	2831	861	4	–	–
J1827.7+1141	6470	8506	9998	874	–	–	–
J1829.2+3229	778	1538	1757	579	–	–	–
J1950.2+1215	5497	8100	7723	1660	1	1	–
J2117.6+3725	3852	4953	5870	673	2	2	2
LCO/Sinistro (1-m)							
J0514.6–4406	1741	1915	3194	578	1	1	–
J0737.2–3233	12034	15061	15603	1588	1	1	1
J0933.9–6232	15847	20725	22368	340	–	–	–
J1035.7–6720	12027	12914	21331	213	–	–	–
J1119.9–2204 ^a	890	1778	1634	74	–	–	–
J1231.6–5113	7958	12182	15572	439	5	5	–
LCO/SBIG (0.4-m)							
J1744.1–7619	1045	1711	1440	30	–	–	–
J1757.7–6030	1628	3227	2469	114	–	–	–
J1946.4–5403	1491	1939	1699	115	–	–	–
J2039.9–5618 ^b	1189	1607	937	44	–	–	–

^aAlready identified as a MSP candidate evolving in a MSP-He white dwarf binary by [Swihart et al. \(2022\)](#). In Section 4.4 we explain the non-detection of its optical counterpart as a variable from our survey.

^bAlready identified as a redback candidate by [Romani \(2015\)](#) and [Salveti et al. \(2015\)](#), and confirmed as a γ -ray MSP by [Clark et al. \(2021\)](#). We did not detect this optical variable in our data (see Section 4.4 for details).

Table 3. Optical location, g' , r' and i' -band magnitudes ranges and best estimate of the photometric period for each spider candidate.

Name 3FGL	R.A. (J2000) ^a (h:m:s)	Decl. (J2000) ^a (°: ': ")	Error radius ^b (")	g' band (mag)	r' band (mag)	i' band (mag)	Photometric period (d)
J0737.2–3233	07:36:56.22	–32:32:55.3	0.8	[17.3-17.6]	[16.4-16.6]	[15.9-16.0]	0.3548(5)
J2117.6+3725-A	21:17:56.30	+37:26:44.6	0.9	[19.1-19.5]	[18.2-18.7]	[17.8-18.1]	0.12664(3)
J2117.6+3725-B	21:18:10.14	+37:27:25.7	0.9	[19.0-19.4]	[18.5-18.9]	[18.3-18.7]	0.2209805(8)
J2221.6+6507	22:22:32.80	+65:00:21.0	1.0	[18.9-19.5]	[17.8-18.4]	[17.1-17.8]	0.165(4)

^aThe equatorial coordinates have been obtained using our astrometry-corrected combined image in the r' -band of the corresponding field of view.

^bThe error radius on the optical location has been estimated as FWHM/2 of the corresponding source profile.

in this survey, identified either as eclipsing binaries, pulsating stars or W UMa binaries (see Table C1, for a review about this type of optical variables see Chambliss 1992).

In Figure 2, we plot the average apparent magnitude in the r' -band as a function of the mean dereddened ($r' - i'$) color shown in the light curve from our spider candidates (highlighted in green symbols), together with all the other 17 COBIPULSE periodic variables (shown as orange circles). For comparison, we also include in the same magnitude-color diagram the optical counterparts of all currently known spider systems identified from the *Pan-STARRS* 1 catalog (PS1; Chambers et al. 2016) by Nedreaas (2024) (12 RBs and 9 BWs, shown as red and black circles, respectively). All the ($g' - r'$) and ($r' - i'$) observed colors were corrected into intrinsic (dereddened) colors by using the corresponding color excess value $E(g-r)$ computed for each source from the 3D dust map of Green et al. (2019).

As clearly shown in Figure 2, the COBIPULSE survey is sensitive enough to detect periodicities from sources as faint as $r' \simeq 19$. This indicates that our search is best suited to discover new RB systems. Variable light curves from optically fainter BWs ($r' > 20$) are more difficult to detect with the present survey. Indeed, our candidates (marked in green) are all located in the RB region of the magnitude-color diagram of Figure 2 ($r' \simeq 14 - 20$), suggesting a likely RB nature (see Section 4 for a detailed discussion).

3.1. 3FGL J0737.2–3233

We identify an optical variable and spider candidate (hereafter referred to as J0737) inside both the 95% error ellipses of 3FGL J0737.2–3233 and 4FGL J0736.9–3231 (see Figure 3).

We find from the global minimum of its PDM periodogram a photometric period $P_{\text{best}} = 0.3548 \pm 0.0005$ d (as shown in the left panels of Figure 4), with a FAP probability $< 10^{-4}$ corresponding to a confidence level more than 3σ (see Section 2.3)¹². We fold the g' , r' and i' light curves and color curves on this period using as reference epoch the time $T_0 = 57336.219 \pm 0.002$ MJD, corresponding to the brightness minimum in the r' -

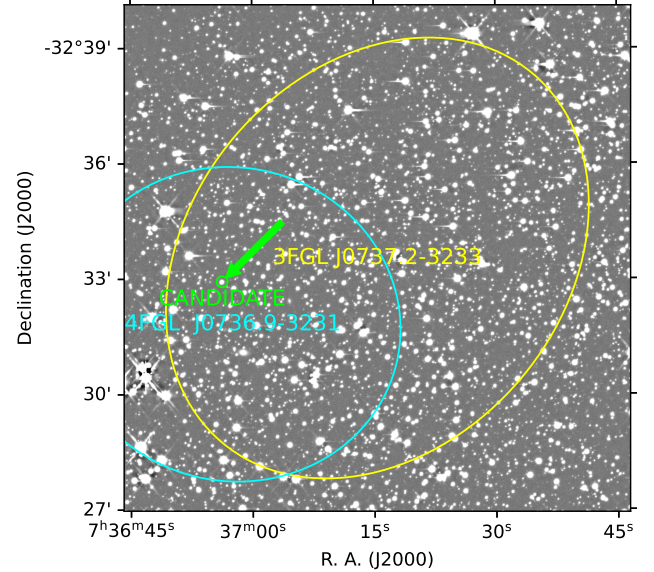


Figure 3. 3FGL J0737.2–3233 field of view observed with LCO/Sinistro. 3FGL and 4FGL 95% error ellipses are shown in yellow and cyan, respectively, while the spider candidate is highlighted in green.

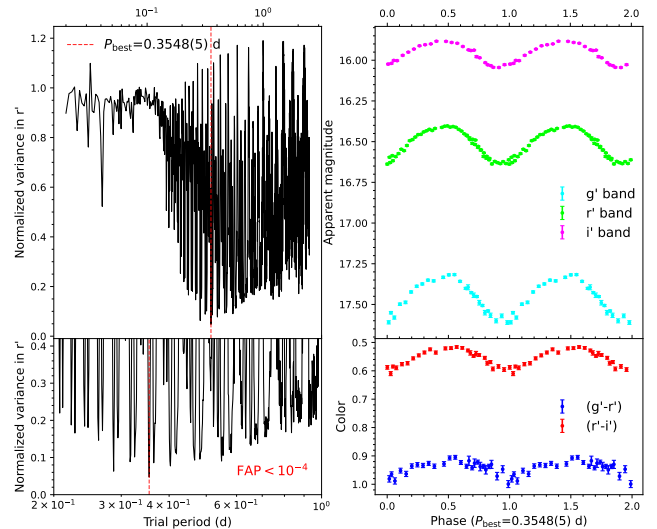


Figure 4. *Top left panel:* PDM periodogram of the r' -band light curve of J0737. *Bottom left panel:* Zoom of the deepest minimum in the periodogram found at $P_{\text{best}} = 0.3548 \pm 0.0005$ d. *Top right panel:* Light curves of J0737 in the g' , r' and i' optical bands folded on P_{best} and reference epoch (minimum light) $T_0 = 57336.219$ MJD, with two cycles shown for displaying purposes. *Bottom right panel:* Observed color curves of J0737 folded on P_{best} .

¹² Here we do not find any of the permuted time series yielding a PDM minimum smaller than the original minimum. Therefore, we place a lower limit on the detection significance. The same consideration applies also for the spider candidates in Section 3.2 and 3.3.

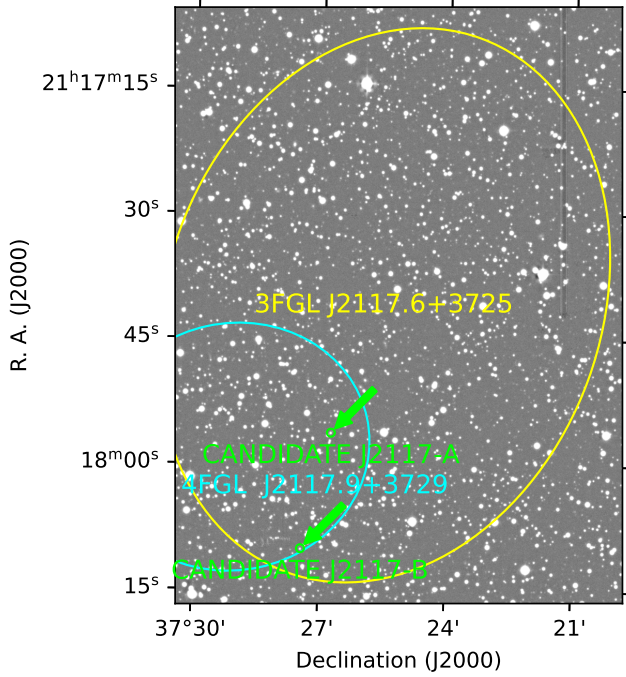


Figure 5. 3FGL J2117.6+3725 field of view observed with INT/WFC. 3FGL and 4FGL 95% error ellipses are shown in yellow and cyan, respectively, while the two spider candidates are highlighted in green.

band¹³ (see right panels of Figure 4). We find the same periodic modulation in all three bands, with peak-to-peak amplitudes of 0.3, 0.2 and 0.2 mag in g' , r' and i' filters, respectively. Additionally, the color curves clearly show a periodic trend, especially $(r' - i')$, peaking around the same phase of maximum flux.

We corrected the observed colors into intrinsic (dereddened) colors, and computed their mean and standard deviation along one full cycle, obtaining $(g' - r') = 0.37 \pm 0.06$ mag and $(r' - i') = 0.15 \pm 0.05$ mag. These two colors have been matched to the spectral templates for low mass stars provided by Allard et al. (2011), which turn out to be compatible with effective temperatures of $T_{\text{eff}} = 6100 \pm 200$ K and $T_{\text{eff}} = 5500 \pm 400$ K for $(g' - r')$ and $(r' - i')$, respectively. Hereinafter, we use this method to estimate the effective temperatures from the optical colors.

Given the shape of its light and color curve shape, in Section 4.1 we discuss J0737 as a likely irradiated RB system observed at a low orbital inclination.

¹³ All the light curves and color curves presented hereafter in this paper have been folded using the time of flux minimum in the r' -band as the reference epoch, as this is supposed to correspond to the companion's inferior conjunction for spider systems.

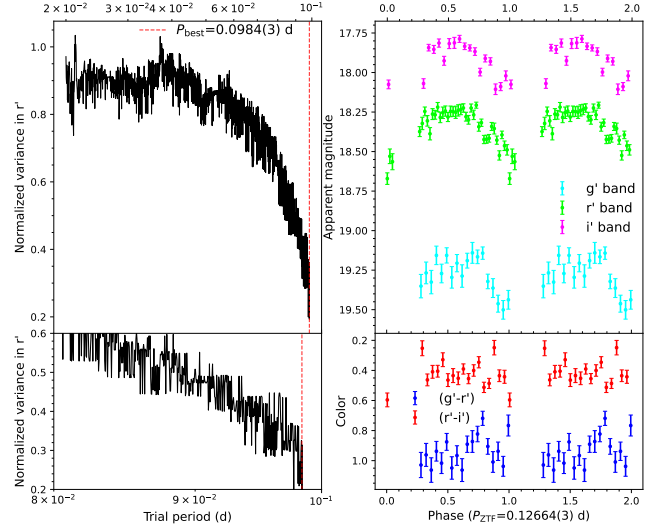


Figure 6. *Top left panel:* PDM periodogram performed on the r' -band light curve of J2117-A. *Bottom left panel:* Zoom of the minimum in the periodogram found at $P_{\text{best}} = 0.0984 \pm 0.0003$ d. *Top right panel:* Light curves of J2117-A in the g' , r' and i' optical bands folded at the photometric period $P_{\text{ZTF}} = 0.12664$ d and reference epoch $T_0 = 59025.415$ MJD, estimated from the periodicity search on ZTF data, where two cycles are shown for displaying purposes. *Bottom right panel:* Observed color curves of J2117-A folded at P_{ZTF} .

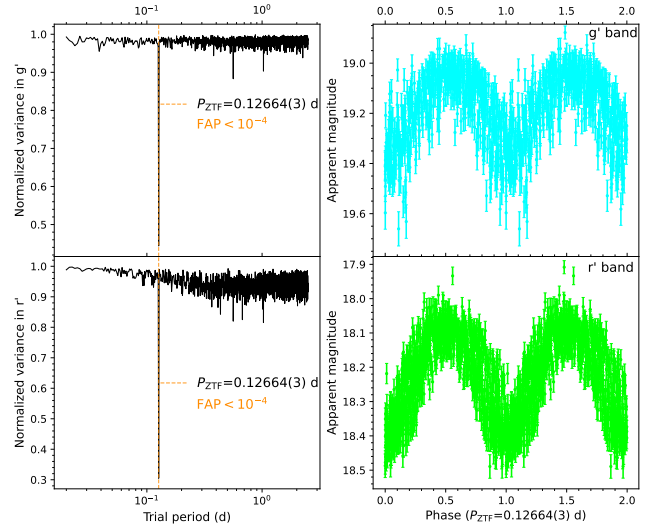


Figure 7. *Left panels:* PDM periodograms performed on the g' and r' -band light curves of J2117-A acquired with ZTF. *Right panels:* ZTF optical light curves of J2117-A folded at the photometric period $P_{\text{ZTF}} = 0.12664$ d and reference epoch $T_0 = 59025.415$ MJD.

3.2. 3FGL J2117.6+3725

We identify two optical variables (hereafter referred to as J2117-A and J2117-B, respectively) inside

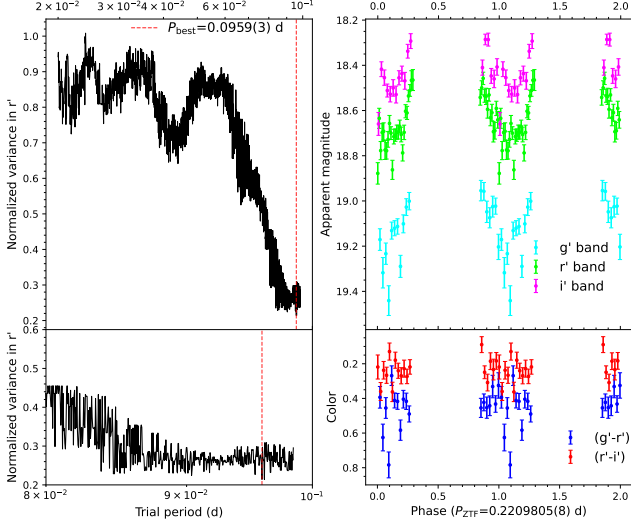


Figure 8. *Left top panel:* PDM periodogram performed on the r' -band light curve of J2117-B. *Left bottom panel:* Zoom of the minimum in the periodogram found at $P_{\text{best}} = 0.0959 \pm 0.0003$ d. *Right top panel:* Light curves of J2117-B in the g' , r' and i' optical bands folded at the photometric period $P_{\text{ZTF}} = 0.2209805$ d and reference epoch $T_0 = 58745.308$ MJD, estimated from the periodicity search on ZTF data, where two cycles are shown for displaying purposes. *Right bottom panel:* Observed color curves of J2117-B folded at P_{ZTF} .

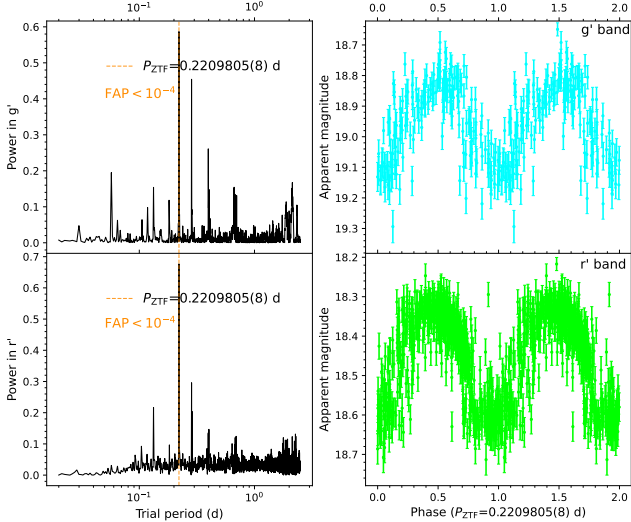


Figure 9. *Left panels:* LS periodograms performed on the g' and r' -band light curves of J2117-B acquired with ZTF. *Right panels:* ZTF optical light curves of J2117-B folded at the photometric period $P_{\text{ZTF}} = 0.2209805$ d and reference epoch $T_0 = 58745.308$ MJD.

both 95% error regions of 3FGL J2117.6+3725 and 4FGL J2117.9+3729, as illustrated in Figure 5.

The periods corresponding to the minima of the PDM periodograms of the INT light curves are $P_{\text{best}} = 0.0984 \pm 0.0003$ d and $P_{\text{best}} = 0.0959 \pm 0.0003$ d for J2117-A and J2117-B, respectively (see left panels of Figures 6 and 8). However, the two periodograms show that the variance is monotonically decreasing towards the right edge of the period grid. This indicates that the observing time window does not cover a full cycle of the two sources, likely indicating incorrect estimates of their periods. Therefore, we instead obtain the periods from PDM and LS periodograms of the ZTF optical light curves (see Section 2.4). The photometric periods for J2117-A and J2117-B are $P_{\text{ZTF}} = 0.12664 \pm 0.00003$ d and $P_{\text{ZTF}} = 0.2209805 \pm 0.0000008$ d, respectively (shown in Figures 7 and 9), both detected with a FAP probability $< 10^{-4}$ and therefore a confidence level of more than 3σ . Here, we used as reference epochs $T_0 = 59025.415 \pm 0.002$ MJD and $T_0 = 58745.308 \pm 0.002$ MJD, respectively.

These two variables show periodic modulation consistent across different optical bands with amplitudes of 0.3–0.4 mag. We estimated dereddened colors of $(g' - r') = 0.8 \pm 0.1$ mag and $(r' - i') = 0.3 \pm 0.1$ mag for J2117-A, corresponding to temperatures of $T_{\text{eff}} = 4950 \pm 250$ K and $T_{\text{eff}} = 4650 \pm 350$ K, respectively. Applying the same procedure, we obtain for J2117-B $(g' - r') = 0.4 \pm 0.2$ mag and $(r' - i') = 0.17 \pm 0.09$ mag, with respective temperatures of $T_{\text{eff}} = 6300 \pm 600$ K and $T_{\text{eff}} = 5700 \pm 900$ K.

In Section 4.2 we discuss these two variables as potential optical counterparts to RB MSPs dominated by ellipsoidal modulation rather than irradiation, as they show small-amplitude modulations and constant colors.

3.3. 3FGL J2221.6+6507

We detected three optical variables inside the 95% error ellipse of 3FGL J2221.6+6507. Two of these are identified as W UMa eclipsing binary stars in the ZTF catalog (Chen et al. 2020) (see Appendix C, reported in orange as J2221-A and J2221-B in Figure 10), while we classify the other as a spider candidate (henceforth called J2221, green in Figure 10). Here, the location of the 3FGL γ -ray source should be taken with caution, as it is quite close to the Galactic plane (Galactic latitude $b = 6.7^\circ$) and is lacking a 4FGL source association (see discussion in Section 4.3).

We found from the PDM periodogram a periodicity at $P_{\text{best}} = 0.165 \pm 0.004$ d for J2221, which we used to fold our data (see Figure 11). We obtained for this detection a FAP probability $< 10^{-4}$, equivalent to a significance level higher than 3σ . The observed periodic modulation is consistent in the g' , r' and i' bands,

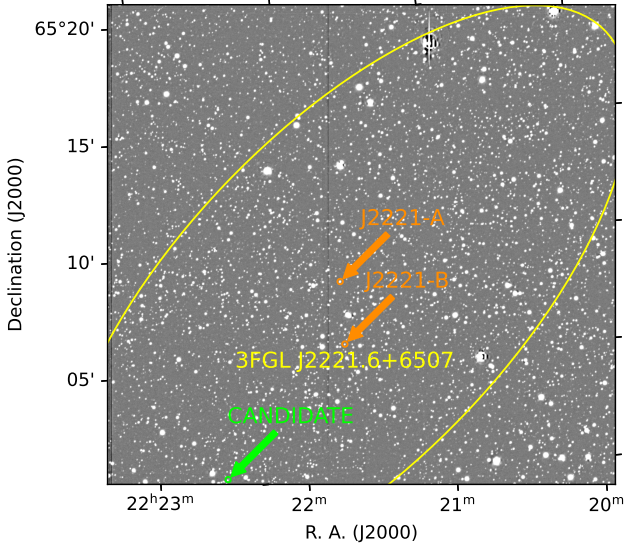


Figure 10. 3FGL J2221.6+6507 field of view observed with STELLA/WiFSIP. 3FGL 95% error ellipse is shown in yellow, while the spider candidate is highlighted in green and the two other periodic variables are reported in orange.

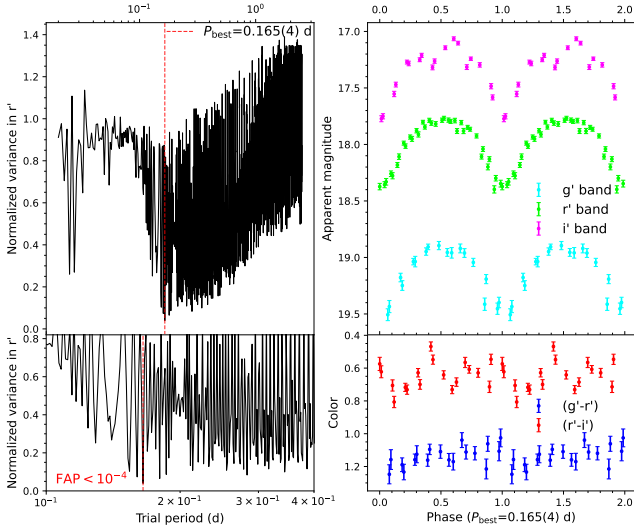


Figure 11. *Top left panel:* PDM periodogram performed on the r' -band light curve of J2221. *Left bottom panel:* Zoom of the deepest minimum in the periodogram found at $P_{\text{best}} = 0.165 \pm 0.004$ d. *Top right panel:* Light curves of J2221 in the g' , r' and i' optical bands folded on P_{best} and reference epoch $T_0 = 57343.939$ MJD, with two cycles shown for displaying purposes. *Bottom right panel:* Observed color curves of J2221 folded on P_{best} .

showing a broad flux maximum and a sharp minimum. We measured peak-to-peak amplitudes of 0.6 mag in all three bands. Also the color curves show a complex variable trend especially in $(r' - i')$, with at least two local maxima at $\phi = 0.5$ and $\phi = 0.75$. We estimate for

the dereddened colors $(g' - r') = 0.5 \pm 0.1$ mag and $(r' - i') = 0.2 \pm 0.1$ mag, which correspond to temperatures of $T_{\text{eff}} = 5850 \pm 350$ K and $T_{\text{eff}} = 5550 \pm 750$ K, respectively.

4. DISCUSSION

4.1. 3FGL J0737.2–3233

We observe a clear periodic pattern in the folded optical light curves of J0737, with consistent color trends, as we can see in Figure 4. This indicates that the star is showing temperature variations along the photometric period $P_{\text{best}} = 0.3548 \pm 0.0005$ d, with a mean temperature of $T_{\text{eff}} = 6100 \pm 200$ K estimated from the dereddened $(g' - r')$ color.

Such features suggest that J0737 is likely a RB system where the companion star is irradiated by the pulsar wind. Thus, the optical light curves have been folded with the presumed orbital period $P_{\text{orb}} = P_{\text{best}} = 0.3548 \pm 0.0005$ d, showing one flux maximum at the superior conjunction of the companion ($\phi = 0.5$). Also, the optical colors peak at $\phi = 0.5$, consistent with the proposed scenario. However, the light curves exhibit peak-to-peak amplitudes of 0.2–0.3 mag, smaller than the ≈ 1 -mag modulations typically observed in RBs undergoing an irradiated regime (see e.g. Linares et al. 2018 for PSR J2215+5135 and Romani & Shaw 2011 for PSR J2339–0533). A low orbital inclination can explain the small amplitudes of the light curves of J0737, implying that we observe only a fraction of the irradiated inner face of the companion at $\phi = 0.5$. This hypothesis is further supported by the small temperature change along the orbit, ~ 200 K, estimated from a base (non-irradiated) temperature of $T_b = 6000 \pm 200$ K at $\phi = 0$ and a day-side (irradiated) temperature of $T_{\text{day}} = 6200 \pm 200$ K at $\phi = 0.5$.

We also found the source 5592027220171664128 from Gaia-DR3 (Gaia Collaboration 2016, 2023) coincident with J0737. The measurement of its parallax, 1.50 ± 0.05 mas, is precise enough to obtain an accurate estimate of the geometric distance to this object. By assuming the distance prior distribution from Bailer-Jones et al. (2021), based on stellar populations, we obtained a distance of $D = 659^{+16}_{-20}$ pc¹⁴. If J0737 is confirmed as a compact MSP, it will be the closest known spider MSP to Earth (considering only parallax distance measurements). Among RB spiders, only PSR J2339–3233 has a similar distance, $D = 750$ pc, estimated via dispersion measure by Ray et al. (2014) using the electron density

¹⁴ We computed the median value and the 1σ lower and upper ends on the geometric distances through http://dc.zah.uni-heidelberg.de/_system_/adql/query/form.

model of Yao et al. (2017). However, its *Gaia* geometric distance is 1.71 kpc. In general, dispersion measure distances systematically underestimate the real spider distances due to small-scale inaccuracies of the electron density map of Yao et al. (2017), as shown by Koljonen et al. (2024).

RB MSPs are generally characterized by X-ray emission produced via synchrotron radiation in the intrabinary shock region (see Section 1), with a typical power-law photon index of $\Gamma \simeq 1\text{--}1.5$ (Linares 2014). In the case of J0737, we did not find any X-ray counterparts in the latest point-source catalogs from *Chandra*, *Swift*, *XMM-Newton* or *eROSITA*. The most constraining X-ray upper limit is obtained from *Swift*/XRT (0.3–10 keV), that observed the corresponding *Fermi* field between 2010 July 31 and 2017 March 6, pointing to J0737 for a total exposure of 10 ks. Using the *Swift*-SXPS query server at <https://www.swift.ac.uk/LSXPS/ulserv.php>, we estimate a 3σ upper limit of 1.5×10^{-3} ct s $^{-1}$ from our source location. Given the low counts upper limit and the proximity of this source, we assume a photon index $\Gamma = 2.5$, larger than typical values for RBs and more suited for low X-ray luminosity spiders (Swihart et al. 2022). Using also an interstellar hydrogen absorption¹⁵ of $N_{\text{H}} = 3.5 \times 10^{21}$ cm $^{-2}$, the corresponding upper limit to the X-ray unabsorbed energy flux¹⁶ is 1.0×10^{-13} erg cm $^{-2}$ s $^{-1}$. Taking the parallax distance reported earlier as a reference value, we obtained an upper limit to the X-ray (0.3–10 keV) luminosity of 5.4×10^{30} ($D/0.7$ kpc) 2 erg s $^{-1}$. For comparison, the X-ray luminosity distribution of Galactic RBs peaks at the higher value of 8×10^{31} erg s $^{-1}$ (Koljonen & Linares 2023). J0737 would then be one of the least luminous RBs in X-rays, which are generally brighter than BWs at these wavelengths (Koljonen & Linares 2023). However, our upper limit still does not rule out a faint X-ray emission from this system, that could be detected with observations deeper than 10 ks.

The match between our optical variable and the pulsar-like *Fermi* unidentified source 3FGL J0737.2–3233, along with its 4FGL association 4FGL J0736.9–3231, as shown in Figure 3, strengthens the identification of J0737 as a RB MSP candidate (for details, see Section 2.1). The integrated 0.1–100 GeV energy flux from 4FGL is $(1.0 \pm 0.1) \times 10^{-11}$ erg cm $^{-2}$ s $^{-1}$, which corresponds to a

γ -ray luminosity of $L_{\gamma} = 5.3 \times 10^{32}$ ($D/0.7$ kpc) 2 erg s $^{-1}$, taking as reference the parallax distance. This value lies within the range of γ -ray luminosities, $\sim 10^{32}\text{--}10^{34}$ erg s $^{-1}$, typically observed from MSPs (Smith et al. 2023).

We also identified an infrared counterpart to J0737, with ID *2MASS* J07365621–3232551 (Skrutskie et al. 2006) and magnitudes $J = 14.31 \pm 0.04$, $H = 13.63 \pm 0.03$, and $K = 13.48 \pm 0.04$. We completed this multi-wavelength search by looking for counterparts in the radio band but did not find any matches from the 1.4 GHz *NRAO VLA Sky Survey* (NVSS, Condon et al. 1998) or the 4.0–10.0 GHz radio follow-up on all 3FGL unassociated sources by Schinzel et al. (2017). Additionally, the other candidates discussed in Sections 4.2 and 4.3 also lack a radio counterpart.

4.2. 3FGL J2117.6+3725

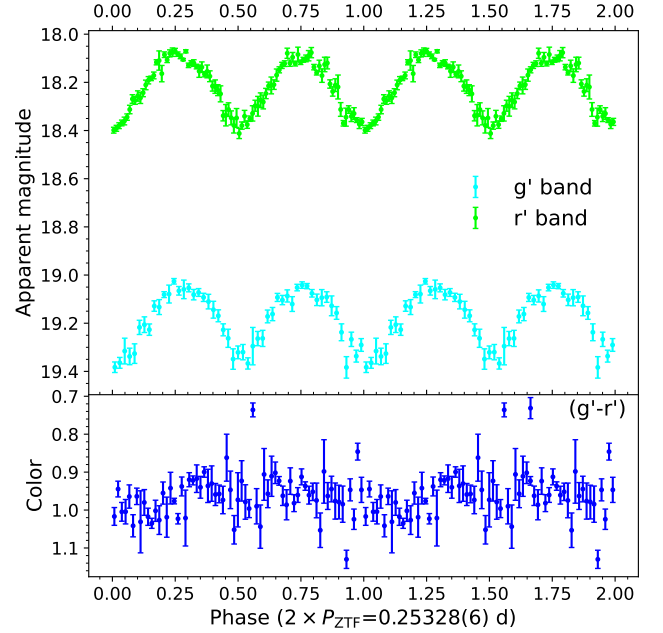


Figure 12. *Top panel:* ZTF g' - and r' -band light curves of J2117-A folded with the assumed orbital period $P_{\text{orb}} = 0.25328$ d and reference epoch $T_0 = 59025.415$ MJD, where two cycles are shown for displaying purposes. *Bottom panel:* Observed ($g' - r'$) color curve of J2117-A.

We find a deep minimum and a strong maximum from the PDM and LS periodograms, respectively, of the ZTF optical light curves of J2117-A and J2117-B, corresponding to the two photometric periods $P_{\text{ZTF}} = 0.12664 \pm 0.00003$ and $P_{\text{ZTF}} = 0.2209805 \pm 0.0000008$ d, respectively (left panels of Figures 7 and 9). The two folded optical light curves show similar periodic shapes, which are consistent in the g' and r' bands, with peak-

¹⁵ Calculated using the H I column density tool at <https://heasarc.gsfc.nasa.gov/cgi-bin/Tools/w3nh/w3nh.pl>.

¹⁶ *Swift*-XRT counts converted into 0.3–10 keV flux using the tool located at <https://heasarc.gsfc.nasa.gov/cgi-bin/Tools/w3pimms/w3pimms.pl>.

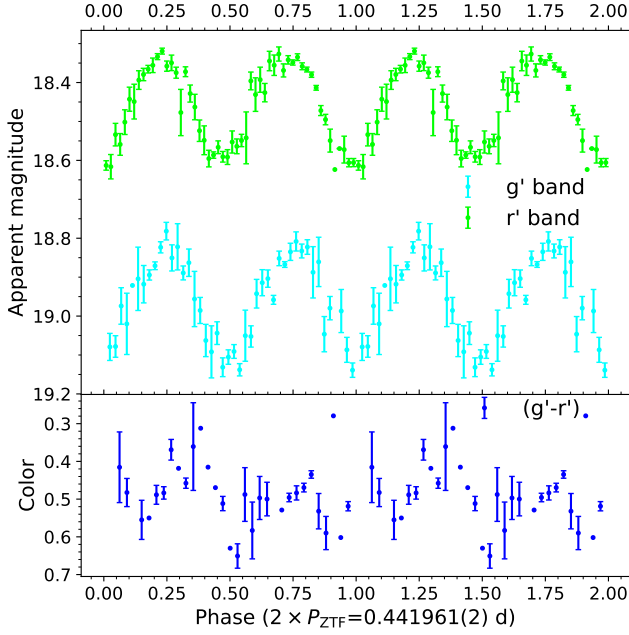


Figure 13. *Top panel:* ZTF g' - and r' -band light curves of J2117-B folded with the assumed orbital period $P_{\text{orb}} = 0.441961$ d and reference epoch $T_0 = 58745.308$ MJD, where two cycles are shown for displaying purposes. *Bottom panel:* Observed $(g' - r')$ color curve of J2117-B.

to-peak amplitudes of 0.4 and 0.3 mag for J2117-A and J2117-B, respectively, illustrated in the right panels of Figures 7 and 9. We also report folded INT light curves for the two variables in the right panels of Figures 6 and 8. Their colors do not show variability consistent with the modulation of the respective light curves, opposite to what is observed in the irradiation case of J0737 (Figure 4). This suggests that both J2117-A and J2117-B do not experience significant temperature variation, with $T_{\text{eff}} = 4950 \pm 250$ K and $T_{\text{eff}} = 6300 \pm 600$ K from $(g' - r')$ color, respectively.

These observations make both systems compatible with being the optical counterpart of a RB MSP not irradiating its companion star, showing only ellipsoidal modulation. Therefore, we show in Figures 12 and 13 their ZTF light curves and color curves now folded with the presumed orbital periods of J2117-A ($P_{\text{orb}} = 2 \times P_{\text{ZTF}} = 0.25328 \pm 0.00006$ d) and J2117-B ($P_{\text{orb}} = 2 \times P_{\text{ZTF}} = 0.441961 \pm 0.000002$ d), obtained as twice their photometric periods. In order to visualize more clearly the periodic pattern, we also rebinned the g' - and r' -band light curves of J2117-A into 50 and 100

phase bins, respectively, while we used 50 bins for both light curves of J2117-B¹⁷.

As we can see from Figures 12 and 13, both rebinned light curves of J2117-A and J2117-B show two flux minima at $\phi = 0.5$ and $\phi = 1$, and two maxima at ascending nodes at $\phi = 0.25$ and $\phi = 0.75$. We do not observe any clear variable trend in the $(g' - r')$ colors of these two systems, which are constant within the errors along their orbits. Both cases closely resemble the optical light curve and color curve shapes typically observed in non-irradiated RBs dominated by ellipsoidal modulation (e.g. PSR J2039–5618, Salvetti et al. 2015; PSR J2129–0429, Bellm et al. 2016 and PSR J1622–0315, Turchetta et al. 2023). In the following, we will thereby consider both J2117-A and J2117-B for our multi-wavelength discussion.

Our candidates J2117-A and J2117-B match two optical sources detected and flagged as variable by *Gaia*, with IDs 1963955610938800896 and 1963954236549278592, respectively (Gaia Collaboration 2023). According to their machine learning algorithm (Rimoldini et al. 2022), the *Gaia* collaboration classifies both these variables as “eclipsing binaries of beta Persei type” (Chambliss 1992). It is interesting to note that the same *Gaia* class is assigned to the variable optical counterparts of known spiders such as the RB PSR J0212+5321 (Perez et al. 2023). Given their respective geometric parallaxes of 0.50 ± 0.11 mas and 0.11 ± 0.13 mas, by using the distance prior from Bailer-Jones et al. (2021) we obtain the distance estimates of $D = 2.2^{+0.6}_{-0.4}$ kpc and $D = 4.5^{+1.5}_{-1.2}$ kpc for J2117-A and J2117-B, respectively.

The latest catalogs from *Chandra*, *Swift*, *XMM-Newton* or *eROSITA* did not provide any X-ray counterparts to our two candidates. *Swift*/XRT observed this field between 2010 September 24 and 2019 October 2 for a total exposure of 3.8 ks. Here we used the same tools and method adopted in Section 4.1 to derive the upper limits to the X-ray fluxes of J2117-A and J2117-B, assuming a photon index $\Gamma = 1.2$ and a hydrogen column density $N_{\text{H}} = 1.6 \times 10^{21} \text{ cm}^{-2}$. We obtained as 3σ upper limits to the counts of these two sources $4.1 \times 10^{-3} \text{ ct s}^{-1}$ and $2.7 \times 10^{-3} \text{ ct s}^{-1}$, which correspond to the upper limits to the unabsorbed energy flux of $2.8 \times 10^{-13} \text{ erg cm}^{-2} \text{ s}^{-1}$ and $1.8 \times 10^{-13} \text{ erg cm}^{-2} \text{ s}^{-1}$ (0.3–10 keV). Using the geometric distances previously estimated for J2117-A and J2117-B, we found as upper limits to the X-ray lu-

¹⁷ We computed the mean magnitude over all the data points included in the corresponding bin, with their standard deviation as uncertainty.

minosity $1.6 \times 10^{32} (D/2.2 \text{ kpc})^2 \text{ erg s}^{-1}$ and $4.3 \times 10^{32} (D/4.5 \text{ kpc})^2 \text{ erg s}^{-1}$, respectively. For comparison, the X-ray luminosity distribution of Galactic RB MSPs peaks at a lower luminosity of $8 \times 10^{31} \text{ erg s}^{-1}$ (Koljonen & Linares 2023). Therefore, our upper limits do not exclude the presence of the X-ray counterparts to these two RB candidates.

As shown in Figure 5, both J2117-A and J2117-B match the γ -ray pulsar-like source 3FGL J2117.6+3725 and also the close 4FGL J2117.9+3729, strengthening their spider association. The 0.1–100 GeV energy flux of the 4FGL object is $(4.3 \pm 1.0) \times 10^{-12} \text{ erg cm}^{-2} \text{ s}^{-1}$, from which we obtained the respective γ -ray luminosities of $L_\gamma = 2.5 \times 10^{33} (D/2.2 \text{ kpc})^2 \text{ erg s}^{-1}$ and $L_\gamma = 1.0 \times 10^{34} (D/4.5 \text{ kpc})^2 \text{ erg s}^{-1}$. Both these estimates are compatible with the typical MSPs luminosities $\sim 10^{32}$ – $10^{34} \text{ erg s}^{-1}$ measured in γ -ray wavelengths (Smith et al. 2023).

Furthermore, we identified an infrared counterpart to J2117-A, with ID *2MASS* J21175634+3726451 (Skrutskie et al. 2006) and magnitudes $J = 16.37 \pm 0.13$, $H = 15.80 \pm 0.15$, and $K = 15.65^{18}$. For the other candidate J2117-B instead we did not find any infrared counterpart from *2MASS* or *AllWISE*.

4.3. 3FGL J2221.6+6507

The folded optical light curves of J2221, reported in Figure 11, show a periodic shape with a sharp flux minimum. Also, the $(g' - r')$ and $(r' - i')$ colors seem variable, peaking within the broad light curve maximum. These color curves indicate temperature variations along the photometric period $P_{\text{best}} = 0.165 \pm 0.004 \text{ d}$ and a mean temperature of $T_{\text{eff}} = 5850 \pm 350 \text{ K}$.

The properties listed above make J2221 a potential RB candidate. Its light curve shape and peak-to-peak amplitude of 0.6 mag suggest a mildly-irradiated companion star. Therefore, the optical light curves have been folded with $P_{\text{orb}} = P_{\text{best}} = 0.165 \pm 0.004 \text{ d}$, the same value as the photometric period, and exhibit one flux maximum at phase $\phi = 0.5$. From Figure 11, we can notice a complex variable trend in the color curves showing at least two local maxima (at $\phi = 0.5$ and $\phi = 0.75$), which is inconsistent with a direct isotropic heating of the companion’s inner face. This, combined with the light maximum flatness and asymmetry with respect to the superior conjunction ($\phi = 0.5$), may suggest hot spots or asymmetric heating for J2221 companion. Similar behaviors have been found and dis-

cussed in previous works for other RBs (e.g. Deneva et al. 2016; Romani & Sanchez 2016; Swihart et al. 2019; Stringer et al. 2021). We obtain for J2221 a base temperature $T_b = 5500 \pm 300 \text{ K}$ and a day-side temperature $T_{\text{day}} = 6000 \pm 350 \text{ K}$ from the $(g' - r')$ colors.

Our candidate is coincident with the variable *Gaia*-DR3 source 2206544469143391872, again ranked in the same category of eclipsing binary as J2117-B from Rimoldini et al. (2022) (see Section 4.2 for details). Using the distance prior distribution from Bailer-Jones et al. (2021), we convert the parallax measurement $0.46 \pm 0.10 \text{ mas}$ of J2221 to a geometric distance of $D = 2.4_{-0.5}^{+0.6} \text{ kpc}$.

No X-ray counterparts or archival observations were found for J2221 from *Chandra*, *Swift*, *XMM-Newton* or *eROSITA*. This optical variable is identified inside the 95% error ellipse of the pulsar-like *Fermi* unidentified source 3FGL J2221.6+6507, which has a γ -ray energy flux of $(9.3 \pm 1.7) \times 10^{-12} \text{ erg cm}^{-2} \text{ s}^{-1}$ (0.1–100 GeV). Using the previous distance estimate as reference, we derived a luminosity of $L_\gamma = 6.1 \times 10^{33} (D/2.4 \text{ kpc})^2 \text{ erg s}^{-1}$, which is compatible with the range of γ -ray luminosities for MSPs (Smith et al. 2023). Although this 3FGL object has a detection significance of 7.4σ , J2221 is missing a 4FGL association, and the closest source 4FGL J2227.1+6455 is located 30' away from our optical location. We deem this suspect detection of 3FGL J2221.6+6507 to be caused by contamination from the Galactic diffuse emission, as this source is quite close to the Galactic plane (Galactic latitude $b = 6.7^\circ$). Indeed, the model of γ -ray diffuse background used in the *Fermi*-3FGL catalog represents the main factor of uncertainties in detections nearby the Galactic plane. This is especially the case for faint sources with spectral energy flux densities peaking at low energies $< 1 \text{ GeV}$ (Acero et al. 2015), like J2221, which has a peak emission of $3.4 \times 10^{-12} \text{ erg cm}^{-2} \text{ s}^{-1}$ in the 0.3–1 GeV band, dropping down to $1.8 \times 10^{-12} \text{ erg cm}^{-2} \text{ s}^{-1}$ at $> 1 \text{ GeV}$. The lack of this source from the 4FGL catalog is likely due to the global improvement of the diffuse emission model with respect to 3FGL. This could undermine the reliability of J2221 as a spider candidate, but we note that a few confirmed spiders lack 4FGL counterparts (e.g. the RB PSR J1723–2837 or the BW PSR J1720–0533, Lindseth 2023).

For completeness, we also report the infrared counterpart to our optical variable, identified as *2MASS* 22223274+6500207 by Skrutskie et al. (2006) with magnitudes $J = 15.49 \pm 0.06$, $H = 14.79 \pm 0.07$, and $K = 14.56 \pm 0.09$.

¹⁸ The uncertainty on the K magnitude is not reported from the *2MASS* catalog in this case due to low quality photometry in this band.

4.4. The MSP candidate 3FGL J1119.9–2204 and the confirmed RB 3FGL J2039.9–5618

While this work was in progress, MSPs were identified in two Fermi sources observed in our survey, 3FGL J1119.9–2204 (Swihart et al. 2022) and 3FGL J2039.9–5618 (Romani 2015; Salvetti et al. 2015). In the following, we briefly discuss why we do not detect any periodic variable in these two fields.

Swihart et al. (2022) identified the likely optical and X-ray counterparts to 3FGL J1119.9–2204, matching also its 4FGL association 4FGL J1120.0–2204. Through optical spectroscopy and radial velocity modeling, they classified this system as a X-ray compact binary, containing a $\approx 0.17 M_{\odot}$ companion star at a temperature of 8650 K, an orbital period of 8.7 h, and a low inclination of $\sim 16^{\circ}$ – 19° . Given these parameter estimates and after binary evolution simulations, Swihart et al. (2022) argue that 4FGL J1120.0–2204 is in an intermediate stage of evolving into an MSP binary with an extremely low-mass white dwarf companion. They also attribute the lack of orbital variability in the optical band to the nearly face-on orientation, the companion underfilling its Roche lobe, and the absence of heating from the pulsar wind. Their interpretation is in agreement with the non-detection of this source as an optical variable in our survey. However, we still detect it as a stable source in all three optical bands, with mean magnitudes of $g' = 15.46 \pm 0.02$, $r' = 15.65 \pm 0.02$, and $i' = 15.73 \pm 0.02$. The detection of a radio or γ -ray MSP from the same location would confirm the scenario proposed by Swihart et al. (2022).

3FGL J2039.9–5618 was identified as a RB candidate by Romani (2015) and Salvetti et al. (2015), who found the X-ray and optical variable counterparts to this Fermi source. Clark et al. (2021) later confirmed this system as a γ -ray MSP. Its optical light curve shows ellipsoidal modulation with an orbital period of 0.22748 ± 0.00043 d (Salvetti et al. 2015) and asymmetry between the two peaks, indicating some residual companion heating. Salvetti et al. (2015) measured mean magnitudes of $g' = 19.40 \pm 0.02$, $r' = 18.71 \pm 0.02$ and $i' = 18.59 \pm 0.02$ for this RB, just above the sensitivity limit of $r' \simeq 19$ attained by the 0.4-m LCO telescope used for our observations. Indeed, we marginally detect this source in the r' -band (at $r' = 18.5 \pm 0.1$), resulting in scarce and low quality photometry with which we cannot assess its variability.

5. CONCLUSIONS

The COBIPULSE survey is aimed at finding new spider MSPs through their variable optical counterparts. To pursue this goal, we performed multi-

band optical observations of 33 promising *Fermi*-3FGL candidates, selected based on their pulsar-like γ -ray properties. This systematic search led to the discovery of four spider candidates, matching 3FGL J0737.2–3233/4FGL J0736.9–3231 (J0737), 3FGL J2117.6+3725/4FGL J2117.9+3729 (J2117-A and J2117-B), and 3FGL J2221.6+6507 (J2221). They all show flux modulations in the sub-day period range, with peak-to-peak amplitudes $\gtrsim 0.3$ mag. We classified all four as likely RB MSP candidates, based on their companion temperatures of 5000–6000 K.

We argue that J0737 is a RB candidate system, with a mean companion temperature of 6100 ± 200 K and an orbital period of 0.3548 ± 0.0005 d. Its variable color curves peaking at the same phase $\phi = 0.5$ as the light maxima, indicate that the companion star is likely irradiated by the pulsar wind. The small-amplitude modulation of 0.2–0.3 mag shown by the J0737 light curves can be explained by a low orbital inclination. If confirmed as a radio or γ -ray MSP, this would be the closest known spider to Earth, with a distance of 659^{+16}_{-20} pc estimated from the *Gaia* parallax measurement. Also, given our 3σ upper limit on the X-ray luminosity of $5.4 \times 10^{30} (D/0.7 \text{ kpc})^2 \text{ erg s}^{-1}$ (0.3–10 keV), J0737 would be one of the least luminous RBs in X-rays.

We identify two optical variables in the field of 3FGL J2117.6+3725 (J2117-A and J2117-B), both exhibiting peak-to-peak amplitudes of 0.3–0.4 mag and constant colors, indicative of small temperature differences of the companion star along the orbit. Thus, we classify both these sources as non-irradiated RB candidates. We estimate for J2117-A and J2117-B respective companion temperatures of 4950 ± 250 K and 6300 ± 600 K, and infer orbital periods of 0.25328 ± 0.00006 d and 0.441961 ± 0.000002 d. Archival X-ray observations only allow us to place shallow upper limits to the X-ray luminosity of $1.6 \times 10^{32} (D/2.2 \text{ kpc})^2 \text{ erg s}^{-1}$ and $4.3 \times 10^{32} (D/4.5 \text{ kpc})^2 \text{ erg s}^{-1}$ for J2117-A and J2117-B, respectively, fully compatible with the presence of an X-ray counterpart not detected yet.

We deem J2221 as a RB MSP candidate, with a mean companion temperature of 5850 ± 350 K and an orbital period of 0.165 ± 0.004 d. Its variable optical colors peaking within the broad light curve maximum and amplitude of 0.6 mag suggest it to be in a mildly-irradiated regime. We did not find any archival X-ray observations for J2221.

Our work significantly impacts the expansion of the spider population by providing precise sky locations for targeted radio and γ -ray follow-up of four RB candidates, thereby facilitating their detection as MSPs. This is particularly relevant for J0737, J2117-A, and J2117-B,

which we consider to be the strongest of the four candidates we discovered, as discussed earlier. The orbital periods we have estimated will also aid in the accelerated pulsation searches from these systems by narrowing down the parameter space. Phase resolved optical spectroscopy will help confirming the nature of these sources and determine their fundamental parameters.

ACKNOWLEDGMENTS

This project has received funding from the European Research Council (ERC) under the European Union’s Horizon 2020 research and innovation programme (grant agreement No. 101002352, PI: M. Linares). This work was supported by the Agencia Estatal de Investigación del Ministerio de Ciencia e Innovación (MCIN/AEI) and the European Regional Development Fund (ERDF) under grant PID2021–124879NB–I00. We thank M. Kennedy for discussions on periodicity search methods and for suggesting the use of the ZTF public data release to extend our dataset. We also thank M. Satybaldiev for his assistance with the method for estimating periods uncertainties. We acknowledge the ASTROSOURCE software developers, in particular M. Fitzgerald for a discussion on ensemble photometry. JC acknowledges support by the Spanish Ministry of Science via the Plan de Generación de conocimiento through grant PID2022-143331NB-I00. P.A.M.P. acknowledges support from grant RYC2021-031173-I funded by MCIN/AEI/ 10.13039/501100011033 and by the ‘European Union NextGenerationEU/PRTR’. This article makes use of observations made in the Observatorios de Canarias del IAC with the STELLA telescope operated on the island of Tenerife by the Leibniz Institute for Astrophysics Potsdam (AIP) in the Observatorio del Teide, and the Isaac Newton Telescope (INT) operated on the island of La Palma by the Isaac Newton Group of Telescopes (ING) in the Observatorio del Roque de los Muchachos. This work is also based on observations from the Las Cumbres Observatory global telescope network, which were performed using the Sinistro camera at the 1-meter LCOGT network and SBIG camera mounted on the 0.4-meter autonomous telescopes at the LCOGT southern sites (Cerro Tololo-CHI, Siding Spring-AUS). This research has made use of the NASA/IPAC Infrared Science Archive, which is funded by the National Aeronautics and Space Administration and operated by the California Institute of Technology. This work has also made use of data from the Zwicky Transient Facility (ZTF). ZTF is supported by the National Science Foundation under Grants No. AST-1440341 and AST-2034437 and a collaboration including current partners Caltech, IPAC, the Weizmann

Institute for Science, the Oskar Klein Center at Stockholm University, the University of Maryland, Deutsches Elektronen-Synchrotron and Humboldt University, the TANGO Consortium of Taiwan, the University of Wisconsin at Milwaukee, Trinity College Dublin, Lawrence Livermore National Laboratories, IN2P3, University of Warwick, Ruhr University Bochum, Northwestern University and former partners the University of Washington, Los Alamos National Laboratories, and Lawrence Berkeley National Laboratories. Operations are conducted by COO, IPAC, and UW.. ZTF is supported by the National Science Foundation under Grants No. AST-1440341 and AST-2034437 and a collaboration including current partners Caltech, IPAC, the Weizmann Institute for Science, the Oskar Klein Center at Stockholm University, the University of Maryland, Deutsches Elektronen-Synchrotron and Humboldt University, the TANGO Consortium of Taiwan, the University of Wisconsin at Milwaukee, Trinity College Dublin, Lawrence Livermore National Laboratories, IN2P3, University of Warwick, Ruhr University Bochum, Northwestern University and former partners the University of Washington, Los Alamos National Laboratories, and Lawrence Berkeley National Laboratories. Operations are conducted by COO, IPAC, and UW. This publication makes use of data products from the Two Micron All Sky Survey, which is a joint project of the University of Massachusetts and the Infrared Processing and Analysis Center/California Institute of Technology, funded by the National Aeronautics and Space Administration and the National Science Foundation. This publication makes use of data products from the Wide-field Infrared Survey Explorer, which is a joint project of the University of California, Los Angeles, and the Jet Propulsion Laboratory/California Institute of Technology, funded by the National Aeronautics and Space Administration. This research has made use of data products from the Pan-STARRS1 Surveys (PS1), which have been made possible through contributions by the Institute for Astronomy at the University of Hawaii, the Pan-STARRS Project Office, the Max-Planck Society and its participating institutes. This work has made use of data products from the European Space Agency (ESA) mission Gaia (<https://www.cosmos.esa.int/gaia>), processed by the Gaia Data Processing and Analysis Consortium (DPAC, <https://www.cosmos.esa.int/web/gaia/dpac/consortium>). Funding for the DPAC has been provided by national institutions, in particular the institutions participating in the Gaia Multilateral Agreement. This research has made use of data products from the Catalina Sky Survey (CSS), specifically the Catalina Sky Survey Periodic Variables Catalog.

NNG05GF22G issued through the Science Mission Directorate Near-Earth Objects Observations Program. This work also used data products from the ATLAS project. The ATLAS project is primarily funded by NASA under grant number NN12AR55G, and it is operated by the Institute for Astronomy at the University of Hawaii. We also used data and/or software provided by the High Energy Astrophysics Science Archive Research Center, which is a service of the Astrophysics Science Division at NASA and Goddard Space Flight Center. This work made use of data supplied by the UK Swift Science Data Centre at the University of Leicester. This research used also data from the 4XMM-DR13s catalog, created from observations obtained with XMM-Newton,

an ESA science mission with instruments and contributions directly funded by ESA Member States and NASA.

DATA AVAILABILITY

The raw STELLA, INT and LCO images with bias and flats frames used for data reduction can be obtained by contacting M. Turchetta. ZTF data are public and can be obtained through the IRSA light curve service https://irsa.ipac.caltech.edu/docs/program_interface/ztf_lightcurve_api.html.

Facilities: STELLA:1.5m/WiFSIP, INT:2.5m/WFC, LCO:1m/Sinistro, LCO:0.4m/SBIG, IRSA, PO:1.2m

Software: IRAF (Tody 1986), SEP (Barbary et al. 2016), Source Extractor (Bertin & Arnouts 1996), ASTROSOURCE (Fitzgerald et al. 2021)

REFERENCES

- Acero, F., Ackermann, M., Ajello, M., et al. 2015, ApJS, 218, 23, doi: [10.1088/0067-0049/218/2/23](https://doi.org/10.1088/0067-0049/218/2/23)
- Ackermann, M., Ajello, M., Allafort, A., et al. 2012, The Astrophysical Journal, 753, 83, doi: [10.1088/0004-637X/753/1/83](https://doi.org/10.1088/0004-637X/753/1/83)
- Allard, F., Homeier, D., & Freytag, B. 2011, in Astronomical Society of the Pacific Conference Series, Vol. 448, 16th Cambridge Workshop on Cool Stars, Stellar Systems, and the Sun, ed. C. Johns-Krull, M. K. Browning, & A. A. West, 91, doi: [10.48550/arXiv.1011.5405](https://doi.org/10.48550/arXiv.1011.5405)
- Archibald, A. M., Stairs, I. H., Ransom, S. M., et al. 2009, Science, 324, 1411, doi: [10.1126/science.1172740](https://doi.org/10.1126/science.1172740)
- Au, K.-Y., Strader, J., Swihart, S. J., et al. 2023, ApJ, 943, 103, doi: [10.3847/1538-4357/acae8a](https://doi.org/10.3847/1538-4357/acae8a)
- Bailer-Jones, C. A. L., Rybizki, J., Fouesneau, M., Demleitner, M., & Andrae, R. 2021, AJ, 161, 147, doi: [10.3847/1538-3881/abd806](https://doi.org/10.3847/1538-3881/abd806)
- Ballet, J., Bruel, P., Burnett, T. H., Lott, B., & The Fermi-LAT collaboration. 2023, arXiv e-prints, arXiv:2307.12546, doi: [10.48550/arXiv.2307.12546](https://doi.org/10.48550/arXiv.2307.12546)
- Barbary, K., Boone, K., McCully, C., et al. 2016, kbarbary/sep: v1.0.0, v1.0.0, Zenodo, doi: [10.5281/zenodo.159035](https://doi.org/10.5281/zenodo.159035)
- Bassa, C. G., Patruno, A., Hessels, J. W. T., et al. 2014, MNRAS, 441, 1825, doi: [10.1093/mnras/stu708](https://doi.org/10.1093/mnras/stu708)
- Bellm, E. C., Kaplan, D. L., Breton, R. P., et al. 2016, ApJ, 816, 74, doi: [10.3847/0004-637X/816/2/74](https://doi.org/10.3847/0004-637X/816/2/74)
- Bellm, E. C., Kulkarni, S. R., Graham, M. J., et al. 2019, PASP, 131, 018002, doi: [10.1088/1538-3873/aaecbe](https://doi.org/10.1088/1538-3873/aaecbe)
- Bertin, E., & Arnouts, S. 1996, A&AS, 117, 393, doi: [10.1051/aas:1996164](https://doi.org/10.1051/aas:1996164)
- Bhattacharya, D., & van den Heuvel, E. P. J. 1991, PhR, 203, 1, doi: [10.1016/0370-1573\(91\)90064-S](https://doi.org/10.1016/0370-1573(91)90064-S)
- Brown, T. M., Baliber, N., Bianco, F. B., et al. 2013, PASP, 125, 1031, doi: [10.1086/673168](https://doi.org/10.1086/673168)
- Chambers, K. C., Magnier, E. A., Metcalfe, N., et al. 2016, arXiv e-prints, arXiv:1612.05560, doi: [10.48550/arXiv.1612.05560](https://doi.org/10.48550/arXiv.1612.05560)
- Chambliss, C. R. 1992, Publications of the Astronomical Society of the Pacific, 104, 663, doi: [10.1086/133036](https://doi.org/10.1086/133036)
- Chen, X., Wang, S., Deng, L., et al. 2020, The Astrophysical Journal Supplement Series, 249, 18, doi: [10.3847/1538-4365/ab9cae](https://doi.org/10.3847/1538-4365/ab9cae)
- Clark, C. J., Nieder, L., Voisin, G., et al. 2021, MNRAS, 502, 915, doi: [10.1093/mnras/staa3484](https://doi.org/10.1093/mnras/staa3484)
- Condon, J. J., Cotton, W. D., Greisen, E. W., et al. 1998, AJ, 115, 1693, doi: [10.1086/300337](https://doi.org/10.1086/300337)
- D’Amico, N., Possenti, A., Manchester, R. N., et al. 2001, ApJL, 561, L89, doi: [10.1086/324562](https://doi.org/10.1086/324562)
- Deneva, J. S., Ray, P. S., Camilo, F., et al. 2016, ApJ, 823, 105, doi: [10.3847/0004-637X/823/2/105](https://doi.org/10.3847/0004-637X/823/2/105)
- Dodge, O. G., Breton, R. P., Clark, C. J., et al. 2024, MNRAS, 528, 4337, doi: [10.1093/mnras/stae211](https://doi.org/10.1093/mnras/stae211)
- Dodge, O. G., Breton, R. P., Clark, C. J., et al. 2024, Monthly Notices of the Royal Astronomical Society, 528, 4337, doi: [10.1093/mnras/stae211](https://doi.org/10.1093/mnras/stae211)
- Drake, A. J., Djorgovski, S. G., Catelan, M., et al. 2017, Monthly Notices of the Royal Astronomical Society, 469, 3688, doi: [10.1093/mnras/stx1085](https://doi.org/10.1093/mnras/stx1085)

- Evans, I. N., Primini, F. A., Miller, J. B., et al. 2020, in American Astronomical Society Meeting Abstracts, Vol. 235, American Astronomical Society Meeting Abstracts #235, 154.05.
<https://ui.adsabs.harvard.edu/abs/2020AAS...23515405E>
- Evans, P. A., Page, K. L., Osborne, J. P., et al. 2020, The Astrophysical Journal Supplement Series, 247, 54, doi: [10.3847/1538-4365/ab7db9](https://doi.org/10.3847/1538-4365/ab7db9)
- Fitzgerald, M., Gomez, E., Salimpour, S., Singleton, J., & Wibowo, R. 2021, The Journal of Open Source Software, 6, 2641, doi: [10.21105/joss.02641](https://doi.org/10.21105/joss.02641)
- Fruchter, A. S., Stinebring, D. R., & Taylor, J. H. 1988, Nature, 333, 237, doi: [10.1038/333237a0](https://doi.org/10.1038/333237a0)
- Gaia Collaboration. 2016, Astronomy & Astrophysics, 595, A2, doi: [10.1051/0004-6361/201629512](https://doi.org/10.1051/0004-6361/201629512)
- . 2023, A&A, 674, A1, doi: [10.1051/0004-6361/202243940](https://doi.org/10.1051/0004-6361/202243940)
- Gentile, P. A., Roberts, M. S. E., McLaughlin, M. A., et al. 2014, ApJ, 783, 69, doi: [10.1088/0004-637X/783/2/69](https://doi.org/10.1088/0004-637X/783/2/69)
- Gonthier, P. L., Harding, A. K., Ferrara, E. C., et al. 2018, ApJ, 863, 199, doi: [10.3847/1538-4357/aad08d](https://doi.org/10.3847/1538-4357/aad08d)
- Green, G. M., Schlafly, E., Zucker, C., Speagle, J. S., & Finkbeiner, D. 2019, ApJ, 887, 93, doi: [10.3847/1538-4357/ab5362](https://doi.org/10.3847/1538-4357/ab5362)
- Heinze, A. N., Tonry, J. L., Denneau, L., et al. 2018, AJ, 156, 241, doi: [10.3847/1538-3881/aae47f](https://doi.org/10.3847/1538-3881/aae47f)
- Honeycutt, R. K. 1992, PASP, 104, 435, doi: [10.1086/133015](https://doi.org/10.1086/133015)
- Koljonen, K. I. I., & Linares, M. 2023, MNRAS, 525, 3963, doi: [10.1093/mnras/stad2485](https://doi.org/10.1093/mnras/stad2485)
- Koljonen, K. I. I., Lindseth, S. S., Linares, M., Harding, A. K., & Turchetta, M. 2024, Monthly Notices of the Royal Astronomical Society, 529, 575, doi: [10.1093/mnras/stae498](https://doi.org/10.1093/mnras/stae498)
- Linares, M. 2014, ApJ, 795, 72, doi: [10.1088/0004-637X/795/1/72](https://doi.org/10.1088/0004-637X/795/1/72)
- Linares, M. 2020, in Multifrequency Behaviour of High Energy Cosmic Sources - XIII. 3-8 June 2019. Palermo, 23, doi: [10.22323/1.362.0023](https://doi.org/10.22323/1.362.0023)
- Linares, M., & Kachelrieß, M. 2021, JCAP, 2021, 030, doi: [10.1088/1475-7516/2021/02/030](https://doi.org/10.1088/1475-7516/2021/02/030)
- Linares, M., Miles-Páez, P., Rodríguez-Gil, P., et al. 2017, MNRAS, 465, 4602, doi: [10.1093/mnras/stw3057](https://doi.org/10.1093/mnras/stw3057)
- Linares, M., Shahbaz, T., & Casares, J. 2018, ApJ, 859, 54, doi: [10.3847/1538-4357/aabde6](https://doi.org/10.3847/1538-4357/aabde6)
- Lindseth, S. S. 2023, Master's thesis, NTNU. <https://ntnuopen.ntnu.no/ntnu-xmlui/handle/11250/3073819>
- Linnell Nemec, A. F., & Nemec, J. M. 1985, AJ, 90, 2317, doi: [10.1086/113936](https://doi.org/10.1086/113936)
- Lomb, N. R. 1976, Ap&SS, 39, 447, doi: [10.1007/BF00648343](https://doi.org/10.1007/BF00648343)
- McCully, C., Volgenau, N. H., Harbeck, D.-R., et al. 2018, in Society of Photo-Optical Instrumentation Engineers (SPIE) Conference Series, Vol. 10707, Software and Cyberinfrastructure for Astronomy V, ed. J. C. Guzman & J. Ibsen, 107070K, doi: [10.1117/12.2314340](https://doi.org/10.1117/12.2314340)
- Merloni, A., Lamer, G., Liu, T., et al. 2024, A&A, 682, A34, doi: [10.1051/0004-6361/202347165](https://doi.org/10.1051/0004-6361/202347165)
- Nedreaas, I. F. 2024, Master's thesis, NTNU. <https://ntnuopen.ntnu.no/ntnu-xmlui/handle/11250/3143780>
- Nolan, P. L., Abdo, A. A., Ackermann, M., et al. 2012, ApJS, 199, 31, doi: [10.1088/0067-0049/199/2/31](https://doi.org/10.1088/0067-0049/199/2/31)
- Papitto, A., Ferrigno, C., Bozzo, E., et al. 2013, Nature, 501, 517, doi: [10.1038/nature12470](https://doi.org/10.1038/nature12470)
- Perez, K. I., Bogdanov, S., Halpern, J. P., & Gajjar, V. 2023, The Astrophysical Journal, 952, 150, doi: [10.3847/1538-4357/acdc23](https://doi.org/10.3847/1538-4357/acdc23)
- Radhakrishnan, V., & Srinivasan, G. 1982, Current Science, 51, 1096.
<https://ui.adsabs.harvard.edu/abs/1982CS...51.1096R>
- Ray, P. S., Belfiore, A. M., Saz Parkinson, P., et al. 2014, in American Astronomical Society Meeting Abstracts, Vol. 223, American Astronomical Society Meeting Abstracts #223, 140.07.
<https://ui.adsabs.harvard.edu/abs/2014AAS...22314007R>
- Rimoldini, L., Eyer, L., Audard, M., et al. 2022, Gaia DR3 documentation Chapter 10: Variability, Gaia DR3 documentation, European Space Agency; Gaia Data Processing and Analysis Consortium.
<https://ui.adsabs.harvard.edu/abs/2022gdr3.reptE..10R>
- Roberts, M. S. 2012, Proceedings of the International Astronomical Union, 8, 127, doi: [10.1017/S174392131202337X](https://doi.org/10.1017/S174392131202337X)
- Romani, R. W. 2015, ApJL, 812, L24, doi: [10.1088/2041-8205/812/2/L24](https://doi.org/10.1088/2041-8205/812/2/L24)
- Romani, R. W., & Sanchez, N. 2016, ApJ, 828, 7, doi: [10.3847/0004-637X/828/1/7](https://doi.org/10.3847/0004-637X/828/1/7)
- Romani, R. W., & Shaw, M. S. 2011, ApJL, 743, L26, doi: [10.1088/2041-8205/743/2/L26](https://doi.org/10.1088/2041-8205/743/2/L26)
- Salvetti, D., Mignani, R. P., De Luca, A., et al. 2015, ApJ, 814, 88, doi: [10.1088/0004-637X/814/2/88](https://doi.org/10.1088/0004-637X/814/2/88)
- Scargle, J. D. 1982, ApJ, 263, 835, doi: [10.1086/160554](https://doi.org/10.1086/160554)
- Schinkel, F. K., Petrov, L., Taylor, G. B., & Edwards, P. G. 2017, ApJ, 838, 139, doi: [10.3847/1538-4357/aa6439](https://doi.org/10.3847/1538-4357/aa6439)
- Skrutskie, M. F., Cutri, R. M., Stiening, R., et al. 2006, AJ, 131, 1163, doi: [10.1086/498708](https://doi.org/10.1086/498708)
- Smith, D. A., Abdollahi, S., Ajello, M., et al. 2023, ApJ, 958, 191, doi: [10.3847/1538-4357/acee67](https://doi.org/10.3847/1538-4357/acee67)
- Stellingwerf, R. F. 1978, ApJ, 224, 953, doi: [10.1086/156444](https://doi.org/10.1086/156444)
- Stringer, J. G., Breton, R. P., Clark, C. J., et al. 2021, MNRAS, 507, 2174, doi: [10.1093/mnras/stab2167](https://doi.org/10.1093/mnras/stab2167)

- Swihart, S. J., Strader, J., Aydi, E., et al. 2022, ApJ, 926, 201, doi: [10.3847/1538-4357/ac4ae4](https://doi.org/10.3847/1538-4357/ac4ae4)
- Swihart, S. J., Strader, J., Aydi, E., et al. 2021, The Astrophysical Journal, 909, 185
- Swihart, S. J., Strader, J., Chomiuk, L., et al. 2022, The Astrophysical Journal, 941, 199, doi: [10.3847/1538-4357/aca2ac](https://doi.org/10.3847/1538-4357/aca2ac)
- Swihart, S. J., Strader, J., Chomiuk, L., & Shishkovsky, L. 2019, ApJ, 876, 8, doi: [10.3847/1538-4357/ab125e](https://doi.org/10.3847/1538-4357/ab125e)
- Tauris, T. M., Sanyal, D., Yoon, S. C., & Langer, N. 2013, A&A, 558, A39, doi: [10.1051/0004-6361/201321662](https://doi.org/10.1051/0004-6361/201321662)
- Tody, D. 1986, in Society of Photo-Optical Instrumentation Engineers (SPIE) Conference Series, Vol. 627, Instrumentation in astronomy VI, ed. D. L. Crawford, 733, doi: [10.1117/12.968154](https://doi.org/10.1117/12.968154)
- Turchetta, M., Linares, M., Koljonen, K., & Sen, B. 2023, MNRAS, 525, 2565, doi: [10.1093/mnras/stad2435](https://doi.org/10.1093/mnras/stad2435)
- van den Heuvel, E. P. J., & van Paradijs, J. 1988, Nature, 334, 227, doi: [10.1038/334227a0](https://doi.org/10.1038/334227a0)
- Wadiasingh, Z., Venter, C., Harding, A. K., Böttcher, M., & Kilian, P. 2018, ApJ, 869, 120, doi: [10.3847/1538-4357/aaed43](https://doi.org/10.3847/1538-4357/aaed43)
- Webb, N. A., Coriat, M., Traulsen, I., et al. 2020, A&A, 641, A136, doi: [10.1051/0004-6361/201937353](https://doi.org/10.1051/0004-6361/201937353)
- Weber, M., Granzer, T., & Strassmeier, K. G. 2016, in Society of Photo-Optical Instrumentation Engineers (SPIE) Conference Series, Vol. 9910, Observatory Operations: Strategies, Processes, and Systems VI, ed. A. B. Peck, R. L. Seaman, & C. R. Benn, 99100N, doi: [10.1117/12.2232251](https://doi.org/10.1117/12.2232251)
- Wijnands, R., & van der Klis, M. 1998, Nature, 394, 344, doi: [10.1038/28557](https://doi.org/10.1038/28557)
- Yao, J. M., Manchester, R. N., & Wang, N. 2017, ApJ, 835, 29, doi: [10.3847/1538-4357/835/1/29](https://doi.org/10.3847/1538-4357/835/1/29)

APPENDIX

A. COBIPULSE FIELDS OF VIEW

In Figures A1-A3, A4-A5, and A6-A7 we present the combined r' -band images for each field observed with the STELLA, INT, and LCO optical telescopes, respectively. We do not include the 3FGL J0737.2–3233, 3FGL J2117.6+3725, and 3FGL J2221.6+6507 fields since they are already shown in Section 3. We plot the 3FGL 95% error ellipses in yellow, the associated 4FGL 95% error ellipses in cyan, and the 17 periodic variables that we did not attribute to spiders in orange (see Appendix C for details).

B. SELECTION OF OPTICAL VARIABLES

In Figures B1-B6, we report the light curve standard deviation (σ) vs. differential magnitude (Δm) plots for all the optical sources detected separately for each of the 33 COBIPULSE fields of view. We indicate in blue all the “photometric variables” (see Section 2.3), the optical periodic variables not associated to spiders in orange, and the variables classified as spider candidates in green. Most of these plots show a “tick” shape, with a sharp minimum in σ at $\Delta m \approx 2$ mag. This is due to the increasing optical variability observed in fainter sources ($\Delta m \gtrsim 2$ mag), which have less accurate photometry and more scattered data points, even if they are intrinsically stable. Conversely, the brightest sources ($\Delta m \lesssim 2$ mag) show spurious variability, as they are usually close to saturating the CCD detector.

C. PERIODIC VARIABLES

Table C1 lists the optical locations and photometric periods estimated for the 17 periodic variables identified in COBIPULSE. For comparison, we also include the periods measured from other variable catalogs, if any previous identification was present from *CSS* (Drake et al. 2017), *ATLAS* (Heinze et al. 2018), *ZTF* (Chen et al. 2020), or *Gaia*-DR3 (Rimoldini et al. 2022). We also show in Figure C1-C3 the optical light curves for each periodic variable, phase-folded with the photometric period found either from our data (STELLA, INT, or LCO) or from ZTF, in case this was needed to cover a full orbital cycle of the system.

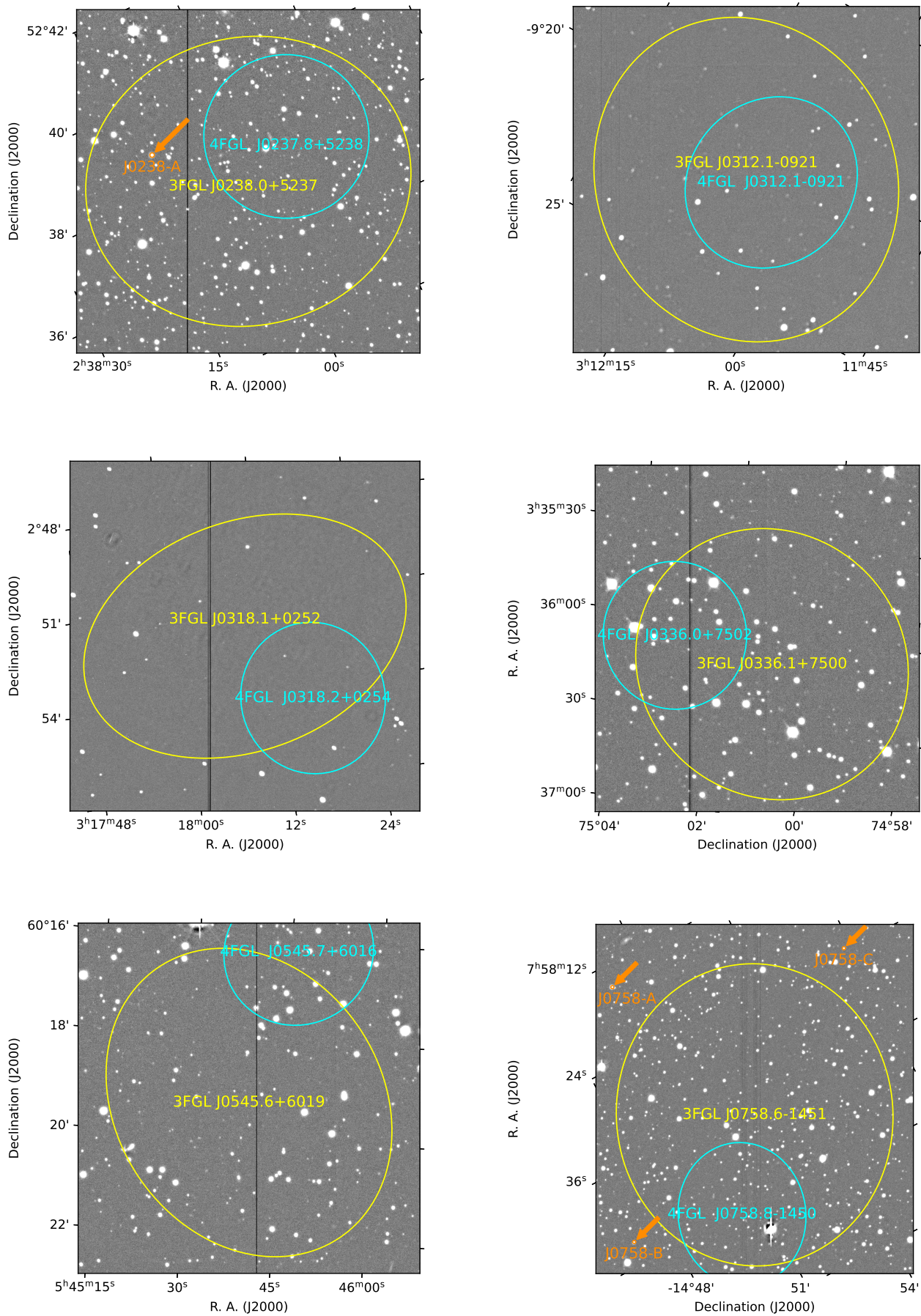


Figure A1. Fermi-3FGL/4FGL fields of view observed with STELLA/WiFSIP (1.2 m).

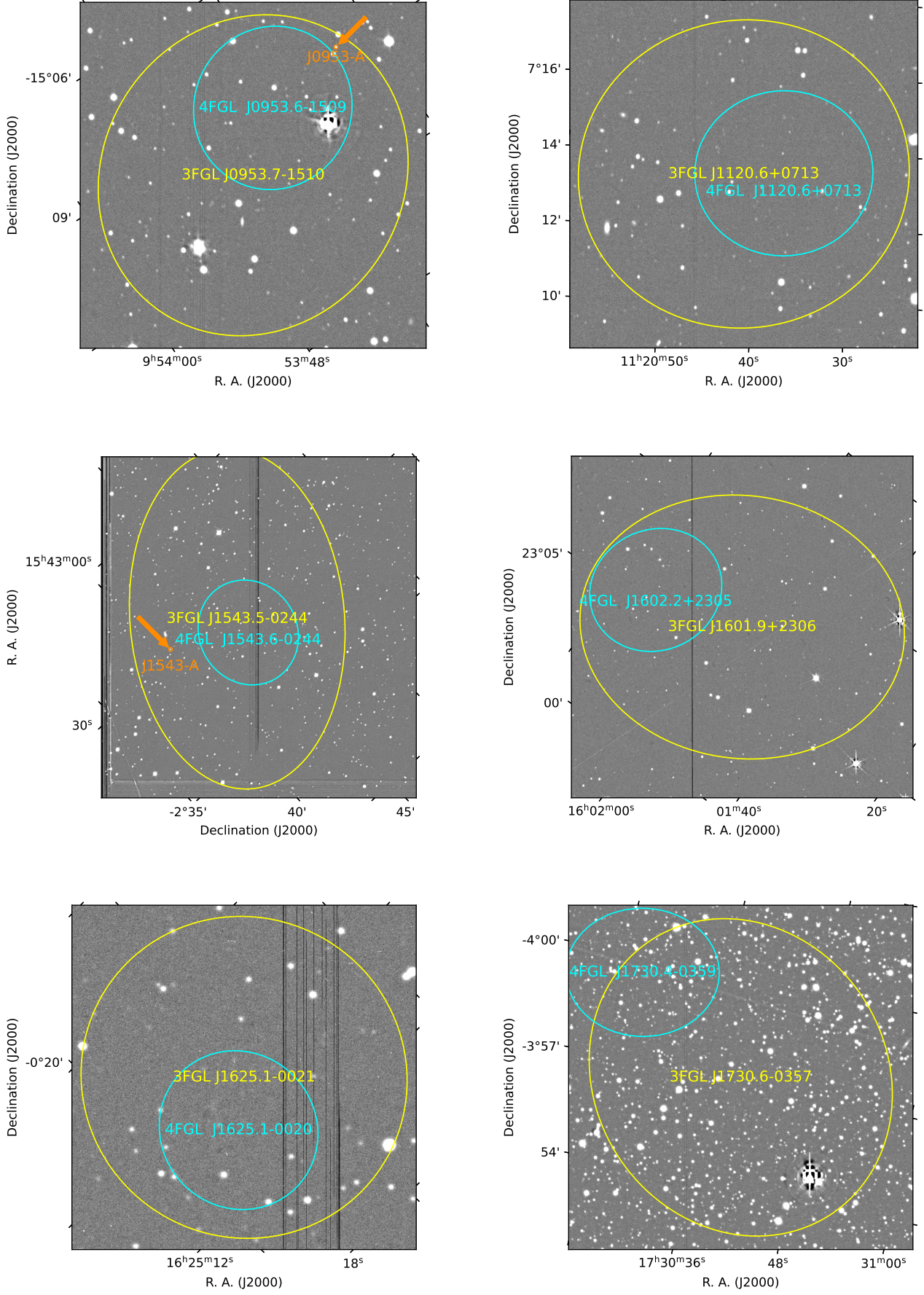


Figure A2. Continued.

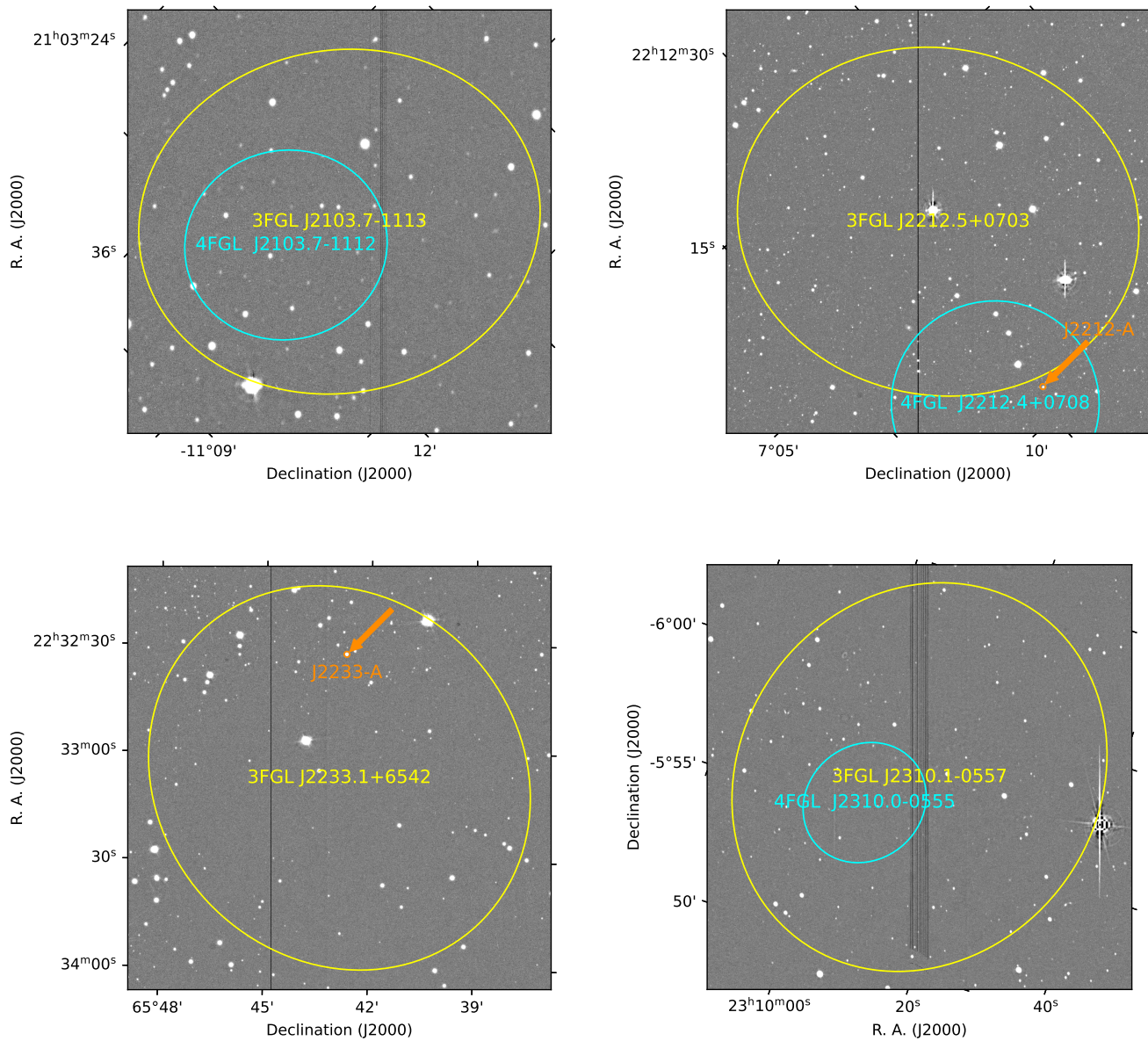


Figure A3. Continued.

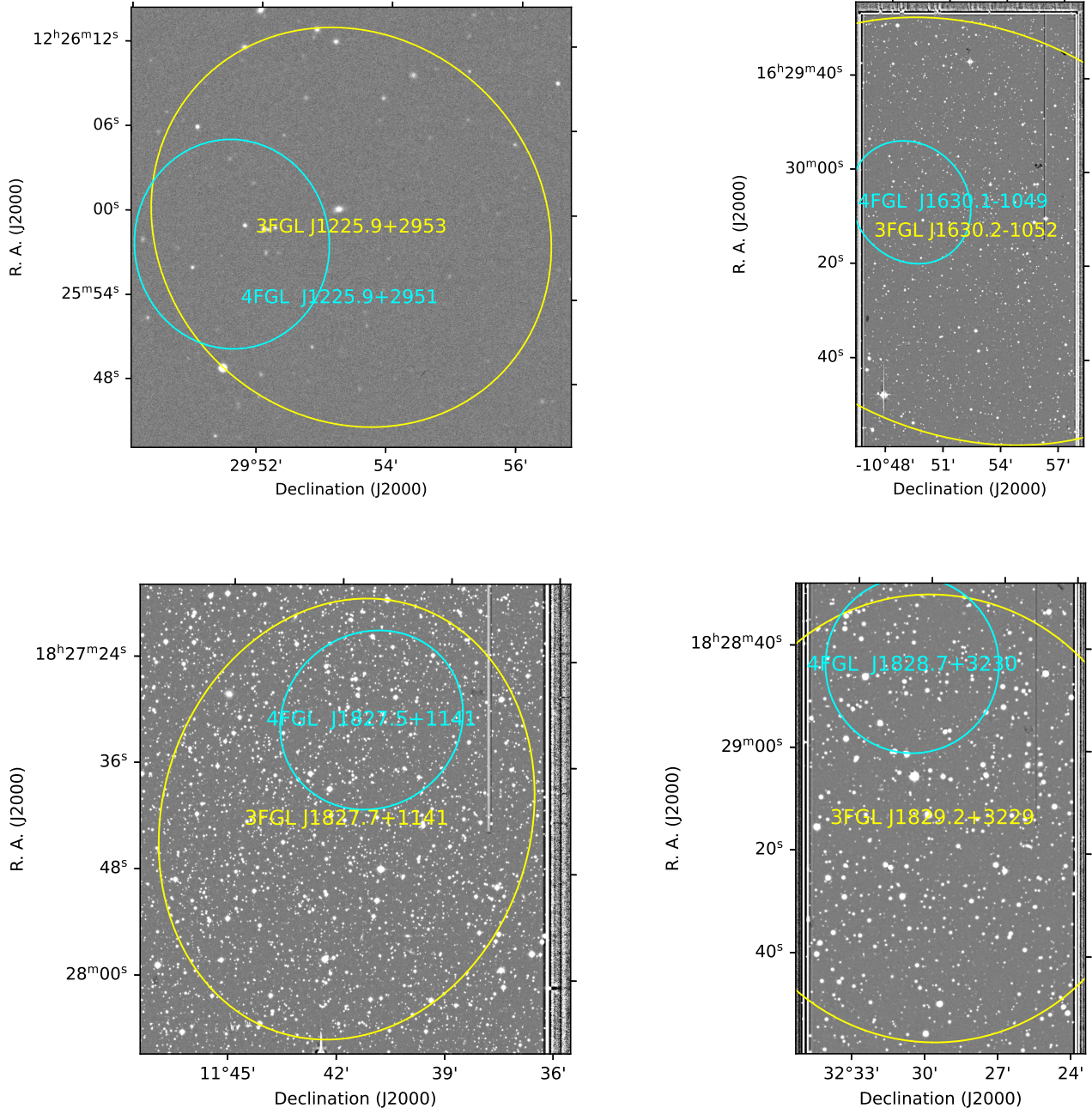


Figure A4. Fermi-3FGL/4FGL fields of view observed with INT/WFC (2.5 m).

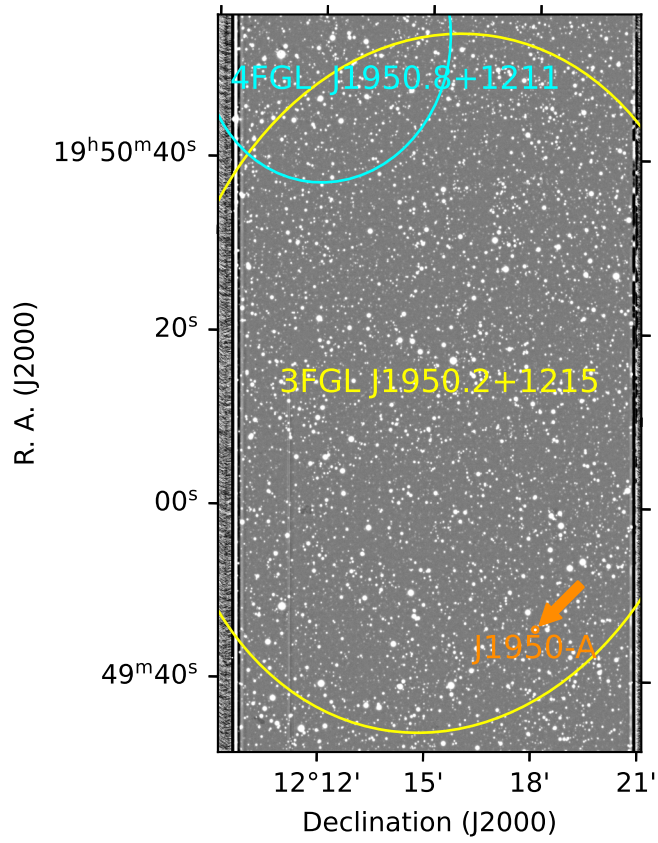


Figure A5. Continued.

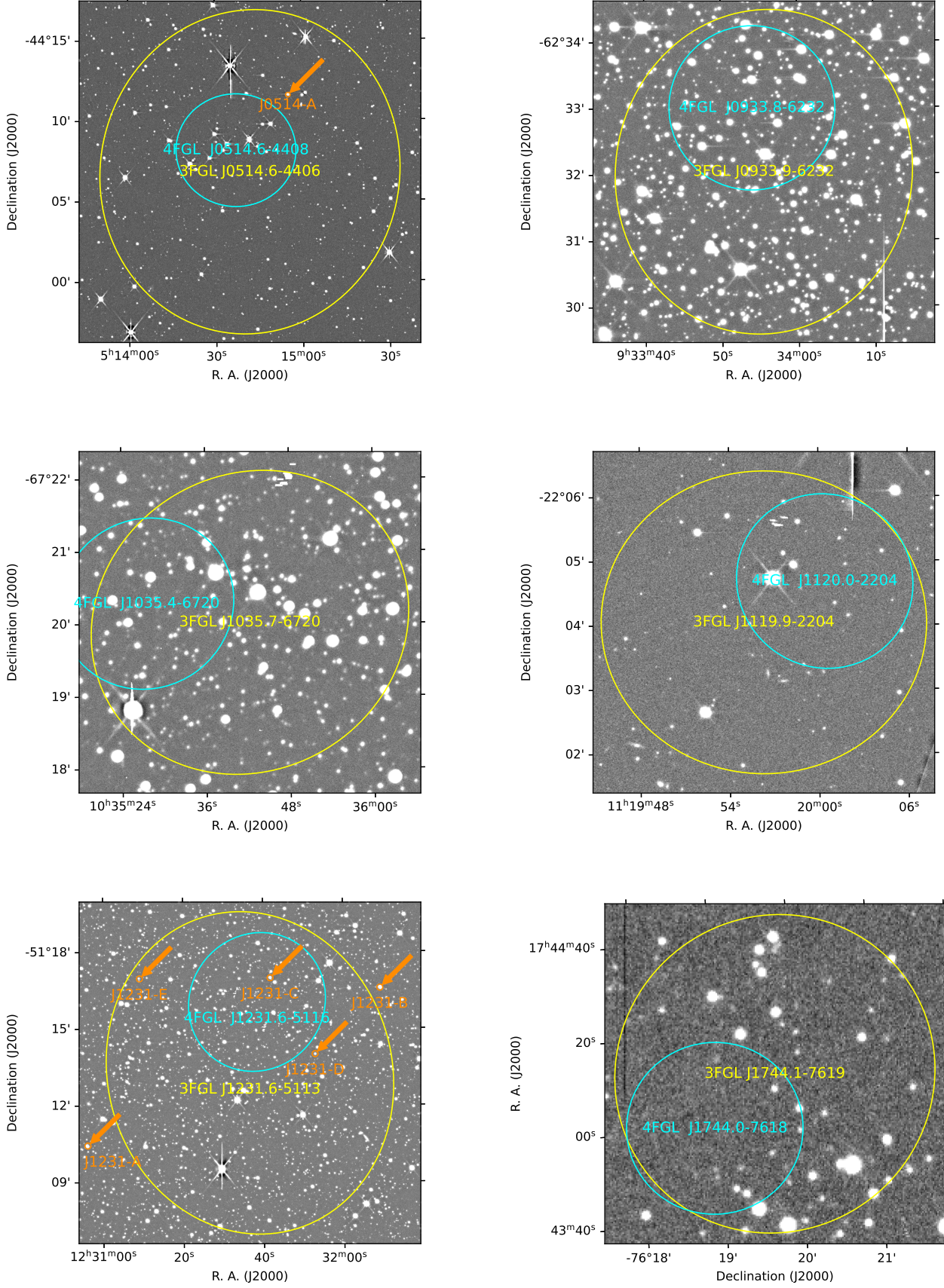


Figure A6. Fermi-3FGL/4FGL fields of view observed with LCO/Sinistro (1 m) and LCO/SBIG (0.4 m).

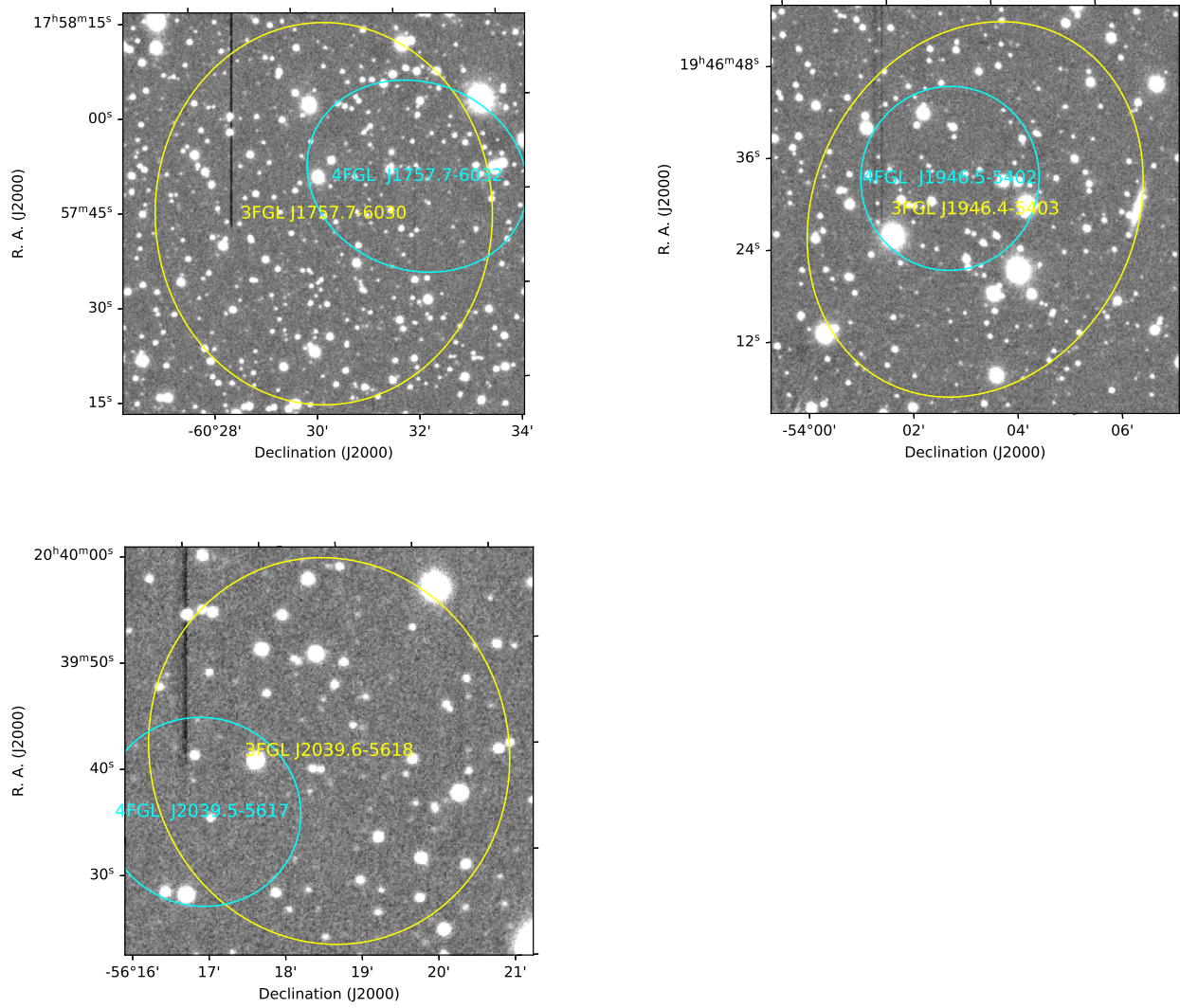


Figure A7. Continued.

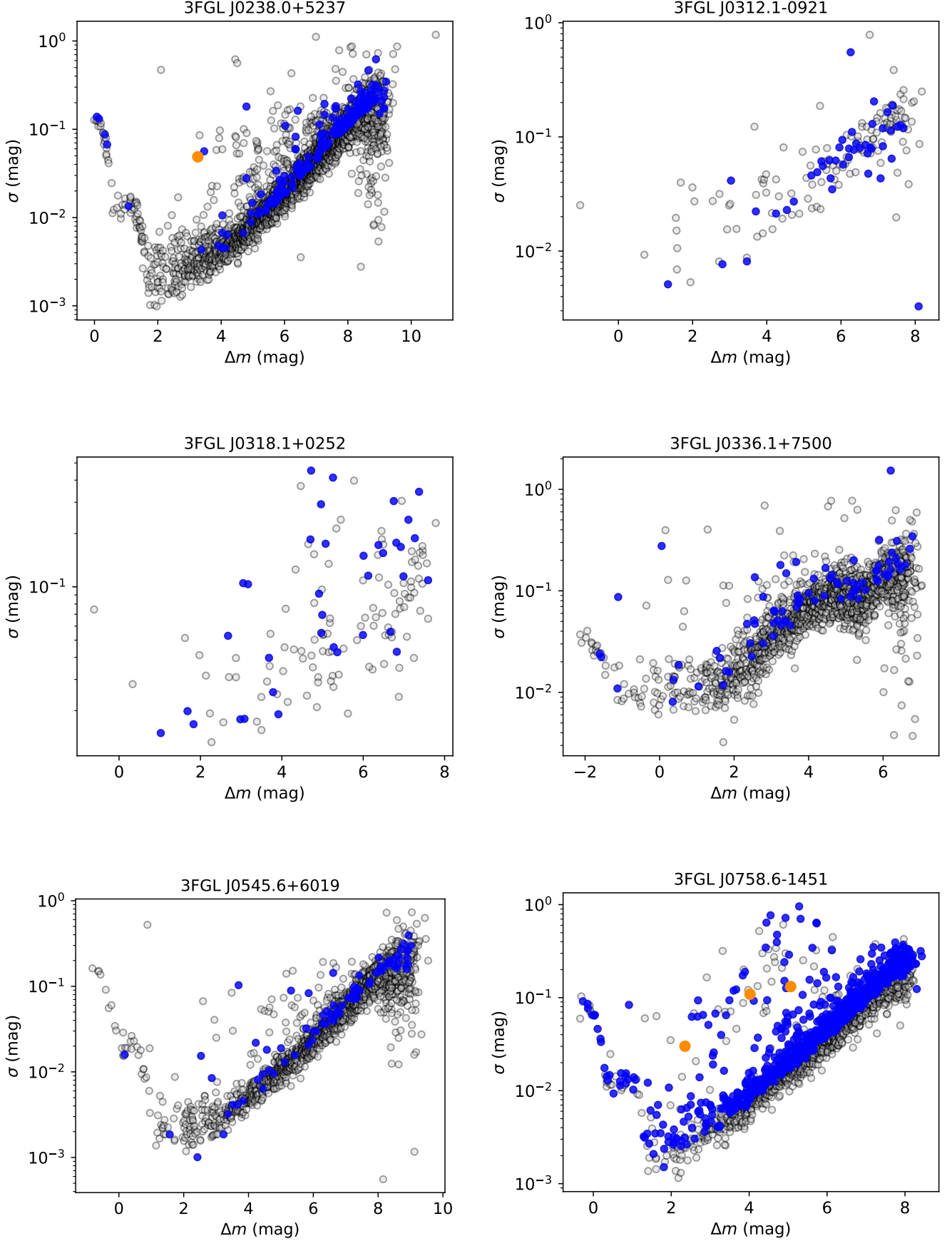


Figure B1. σ vs Δm plots for each of the 33 COBIPULSE fields of view.

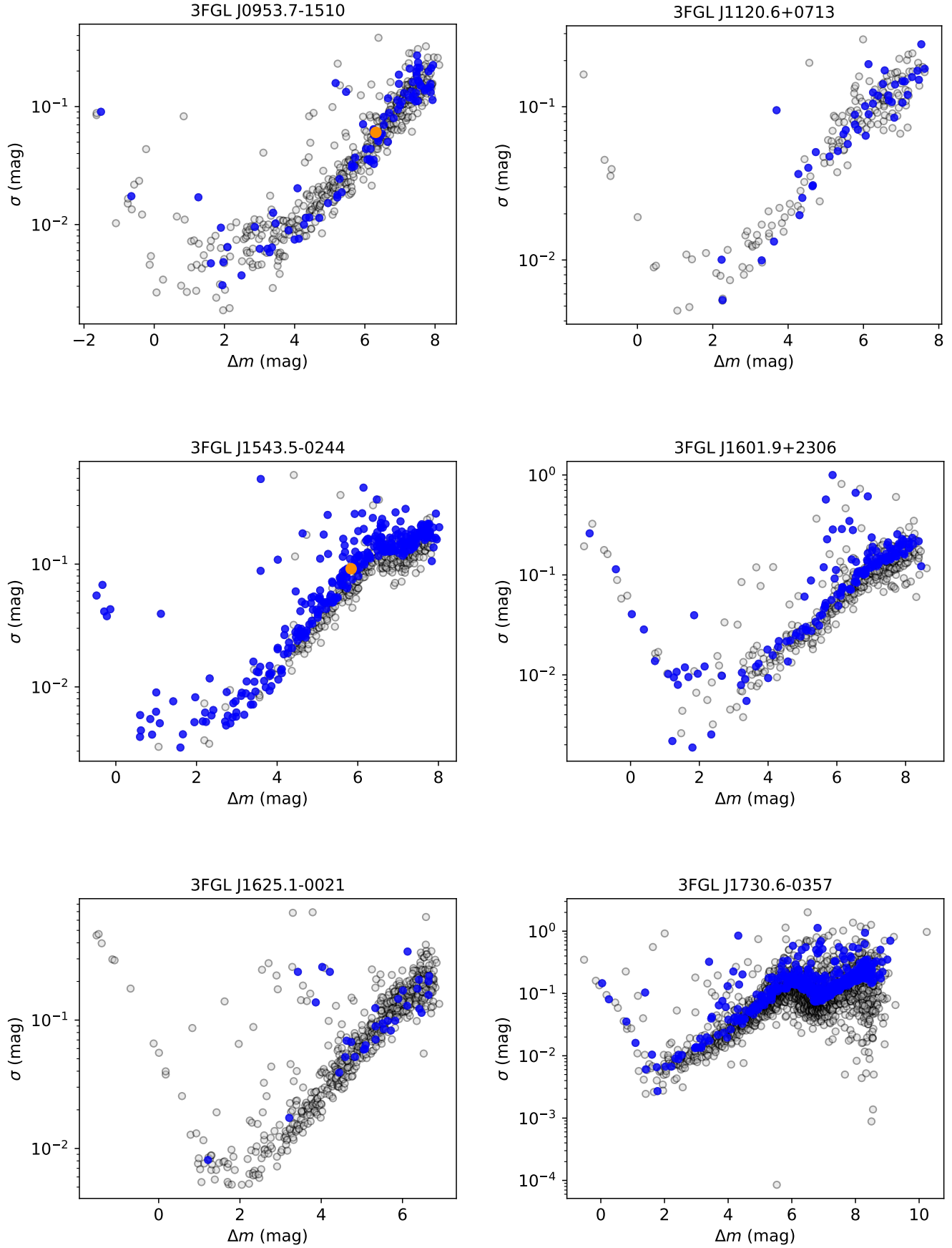


Figure B2. Continued.

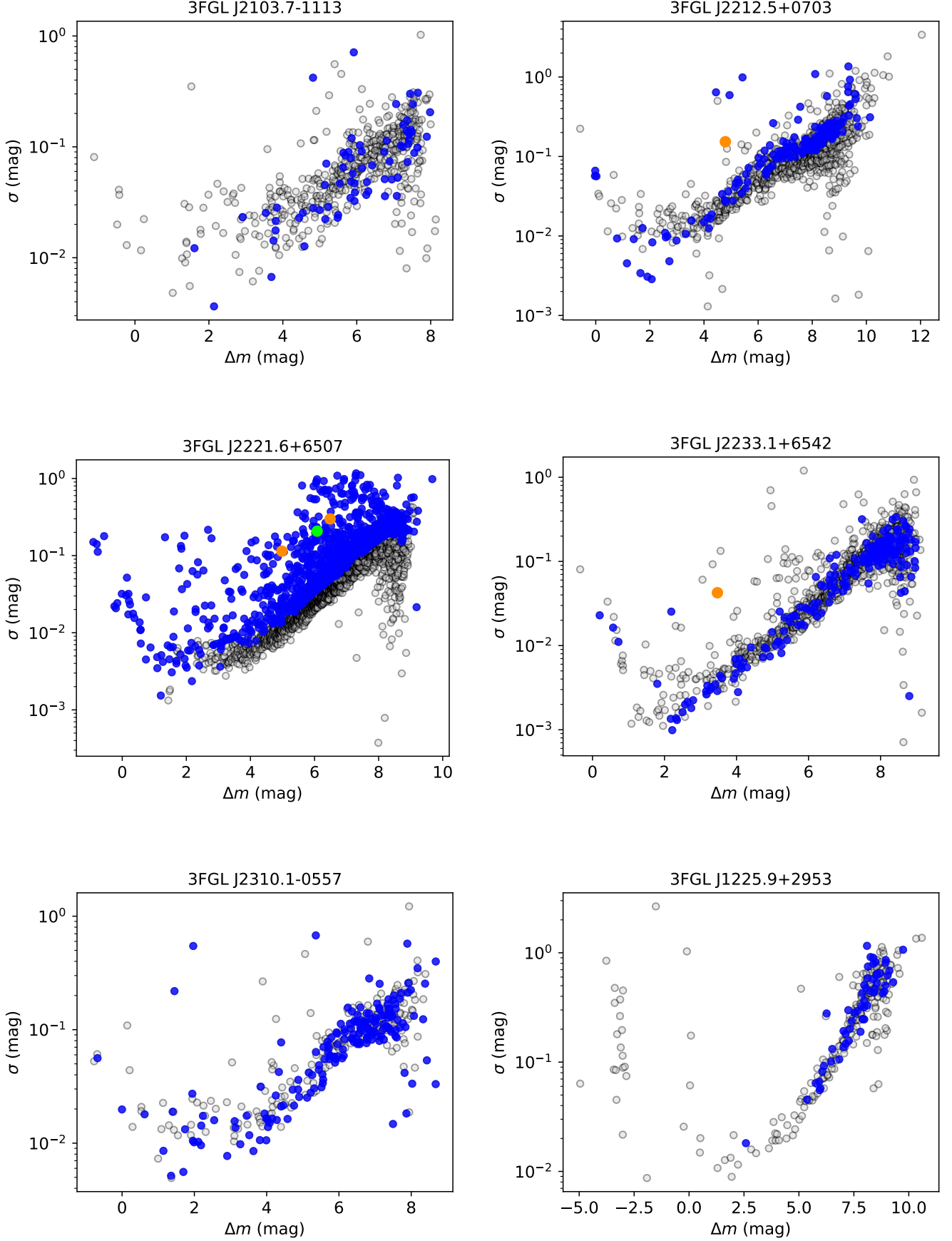


Figure B3. Continued.

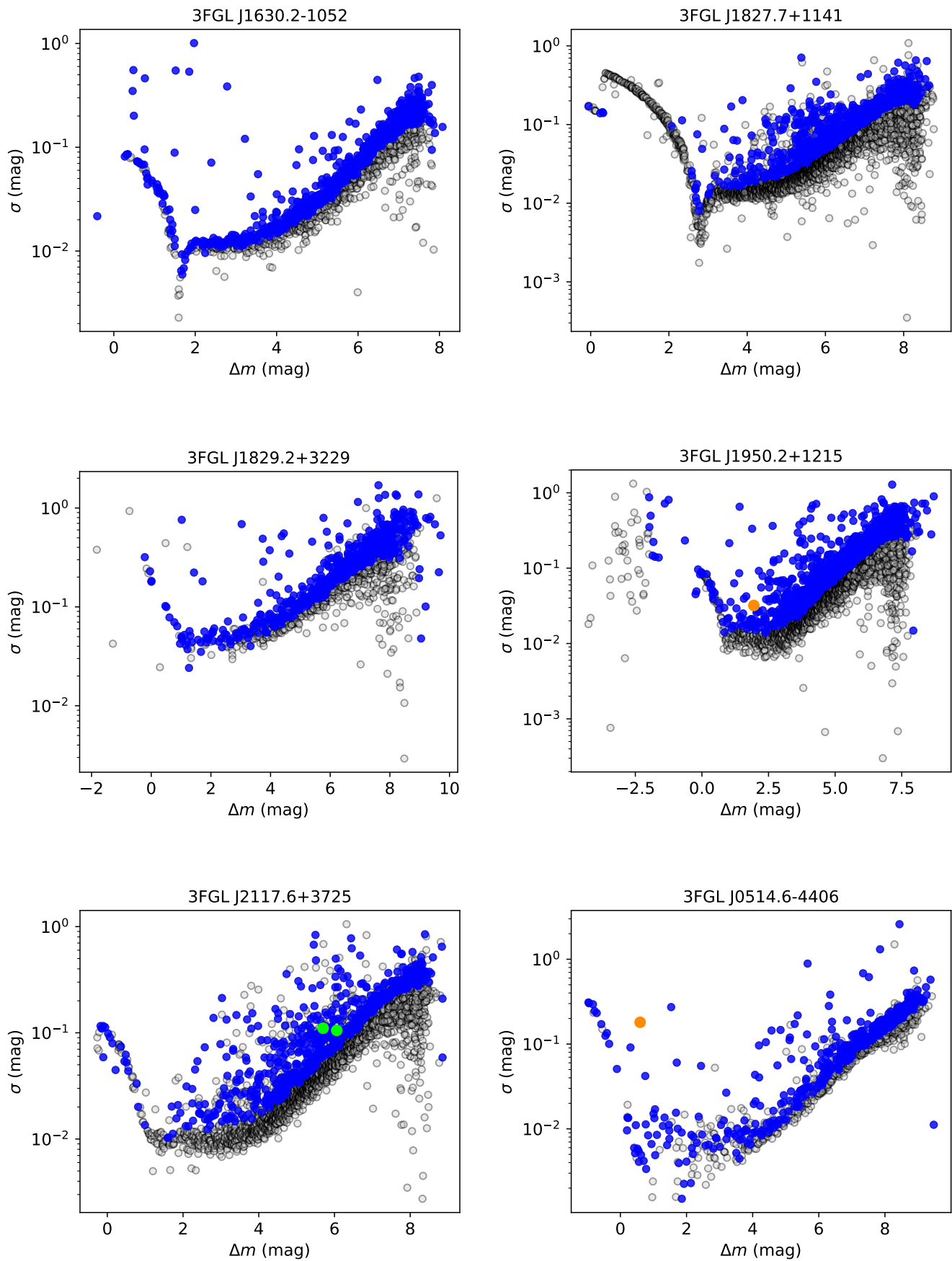


Figure B4. Continued.

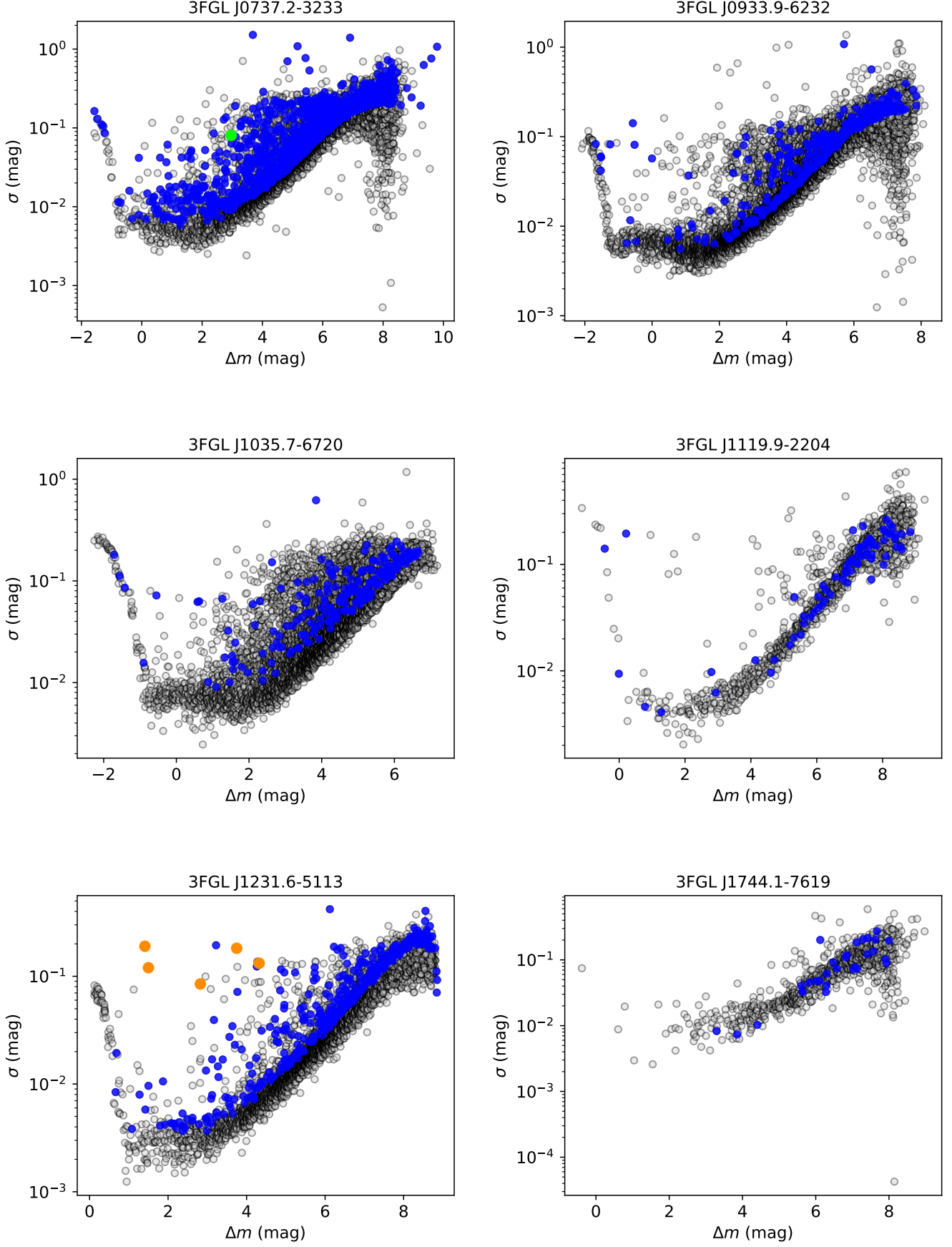


Figure B5. Continued.

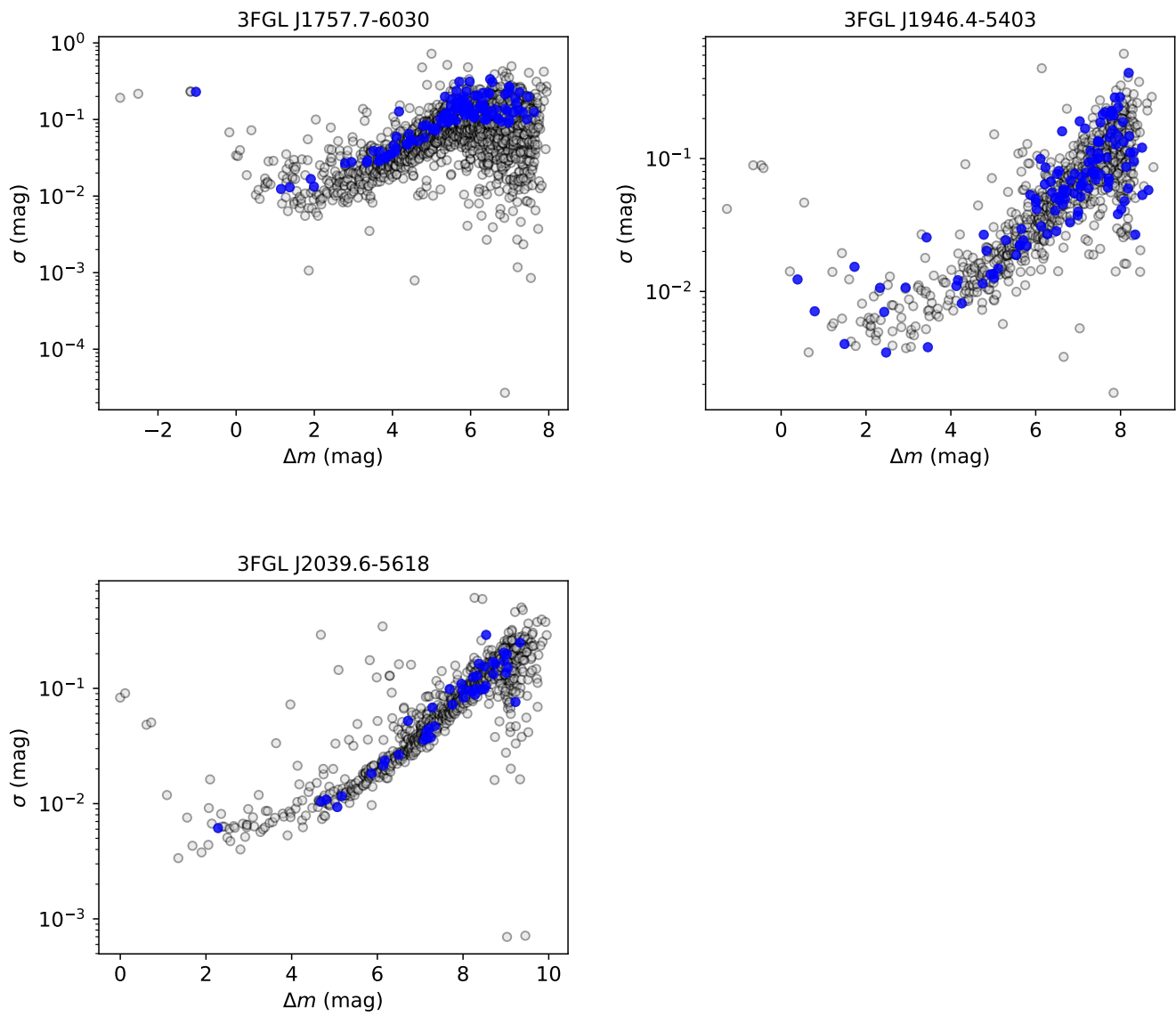


Figure B6. Continued.

Table C1. Optical location, best photometric period from our analysis with uncertainty reported in brackets, and classification with corresponding period measurements from other catalogs for each periodic variable.

Name 3FGL	R.A. (J2000) (h:m:s)	Decl. (J2000) (°: ': ")	Error radius (")	Photometric period (d)	Catalog ID ^a (ID, CLASS)	Catalog period (d)
J0238.0+5237-A	02:38:12.12	+52:38:54.2	0.8	0.3800(5)	<i>ATO</i> J039.5505+52.6484, CBF	0.380069
J0758.6−1451-A	07:58:14.8	−14:49:51	1.0	0.9964(5)	<i>ATO</i> J119.5615−14.8308, LPV	0.996184
J0758.6−1451-B	07:58:45.0	−14:46:52	1.0	0.5351(5)	<i>ATO</i> J119.6874−14.7812, PULSE	0.535069
J0758.6−1451-C	07:58:23.8	−14:56:45	1.0	0.1505(5)	<i>ATO</i> J119.5991−14.9459, CBH	0.165609
J0953.7−1510-A	09:53:28.2	−15:08:52	1.4	0.0957(5)	—	—
J1543.5−0244-A	15:43:27.6	−02:40:31	1.2	0.3176(5)	—	—
J2212.5+0703-A	22:12:31.4	+07:09:08	1.3	0.7640(5)	<i>ATO</i> J333.1308+07.1520, dubious	0.764068
J2221.6+6507-A	22:21:40.7	+65:08:25	1.0	0.5162(5)	<i>ZTF</i> J222140.71+650824.6, EW	0.5161604
J2221.6+6507-B	22:21:40.9	+65:05:43	1.0	0.6586(5)	<i>ZTF</i> J222140.94+650542.6, EW	0.4390726
J2233.1+6542-A	22:32:32.47	+65:42:43.0	0.7	0.4056(5)	<i>ZTF</i> J223232.46+654243.0, EW	0.4056560
J1950.2+1215-A	19:49:45.93	+12:18:06.2	0.9	1.1663(5)	<i>ATO</i> J297.4413+12.3017, DBF	1.166389
J0514.6−4406-A	05:14:55.29	−44:11:34.1	0.9	0.5707(5)	<i>CRTS</i> J051455.2−441132, Ecl	0.570336
J1231.6−5113-A	12:30:00.93	−51:10:26.0	0.7	0.2953(5)	<i>Gaia</i> 6079101525426807808, ECL	0.295279
J1231.6−5113-B	12:32:09.18	−51:16:34.6	0.7	0.2292(5)	<i>Gaia</i> 6079071250193978752, ECL	0.457214
J1231.6−5113-C	12:31:41.77	−51:16:58.5	0.7	0.1854(5)	<i>Gaia</i> 6079072800684576384, ECL	0.370825
J1231.6−5113-D	12:31:52.88	−51:13:59.7	0.7	0.2619(5)	<i>Gaia</i> 6079073213001480192, ECL	0.578556
J1231.6−5113-E	12:31:09.10	−51:16:57.6	0.7	0.1221(5)	<i>Gaia</i> 6079049947157294592, ECL	0.243222

^aID and classification of the periodic variables as found in catalogs (refer to the main text for details). If the field is empty, the source is considered a newly discovered optical variable.

NOTE—Classes of optical variables attributed by the *ATLAS* catalog:

CBF=close binary, full period identified, contact or near-contact eclipsing binary star;

CBH=close binary, half period identified, contact or near-contact eclipsing binary star;

DBF=distant binary, full period identified, detached eclipsing binary star;

LPV=long-period variable that does not seem to fit into any of the *ATLAS* more specific categories;

PULSE=pulsating star showing the classic sawtooth light curve, identified as RR Lyrae, δ Scuti stars, or Cepheids;

dubious=star might not be a real variable.

Classes of optical variables attributed by the *ZTF* catalog:

EW=W UMa-type eclipsing binary star.

Classes of optical variables attributed by the *CSS* catalog:

Ecl=eclipsing binary star.

Classes of optical variables attributed by the *Gaia*-DR3 catalog:

ECL=eclipsing binary star of type beta Persei (Algol).

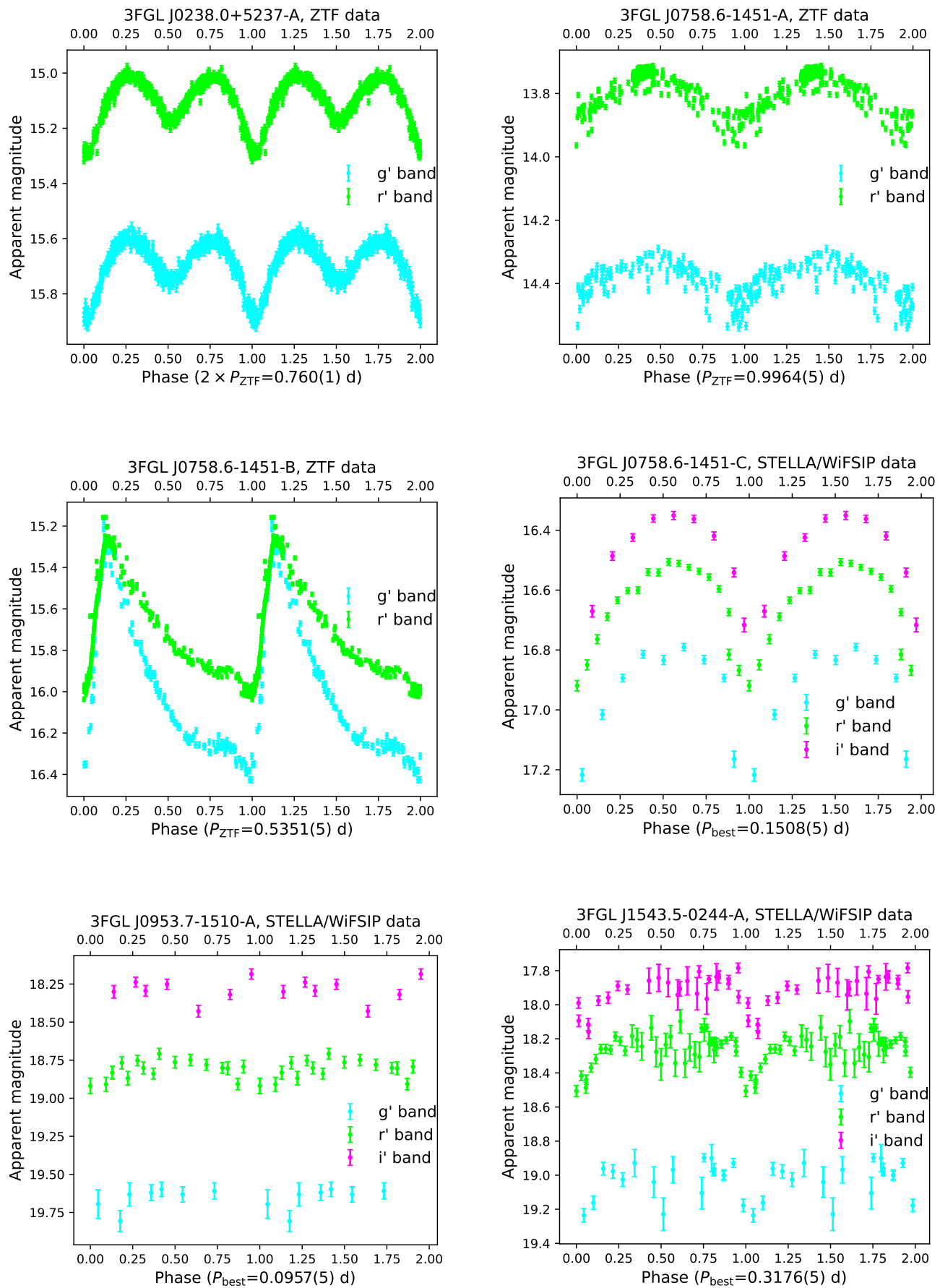


Figure C1. Phase-folded optical light curves for each of the 17 COBIPULSE periodic variables.

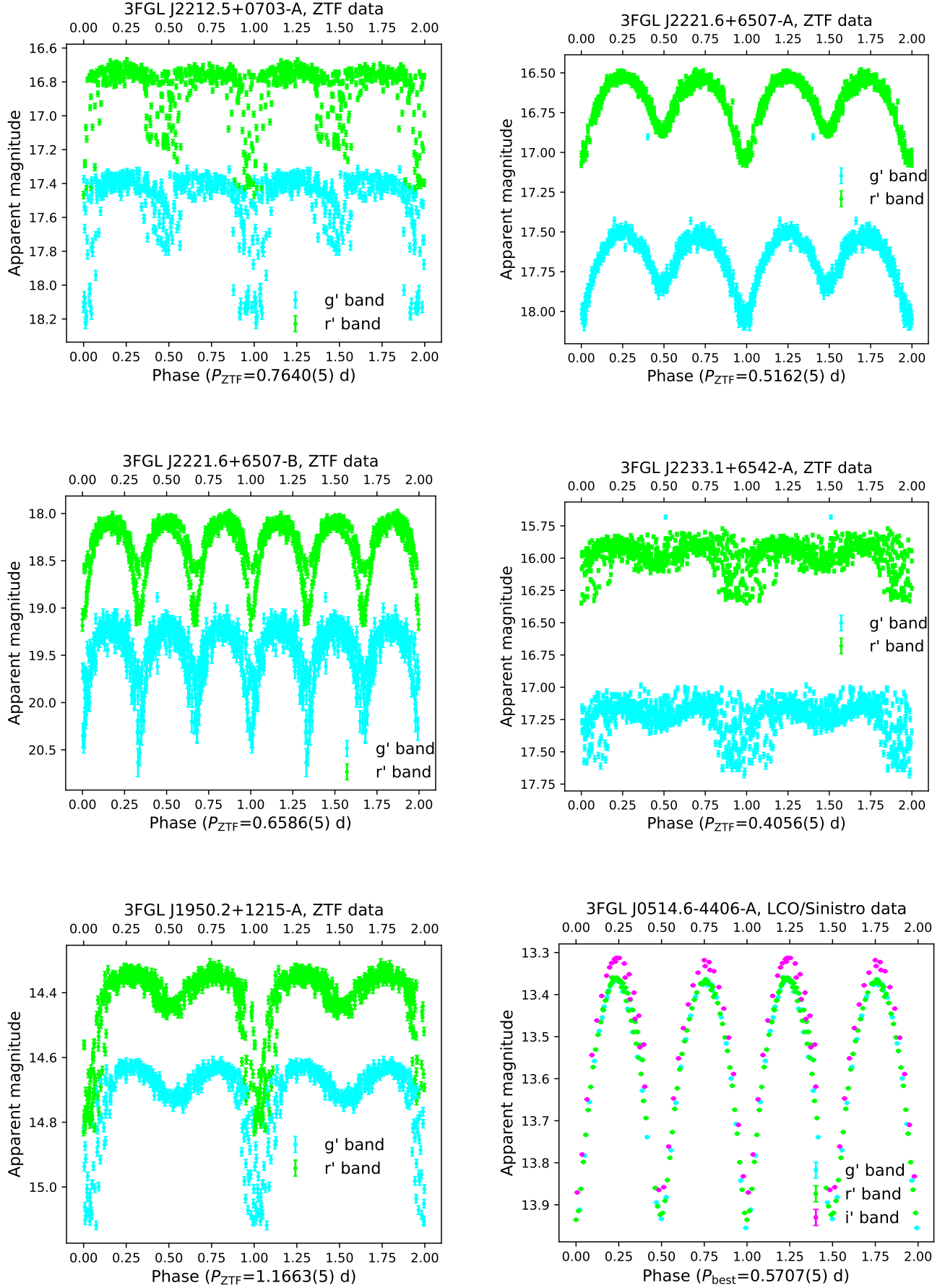


Figure C2. Continued.

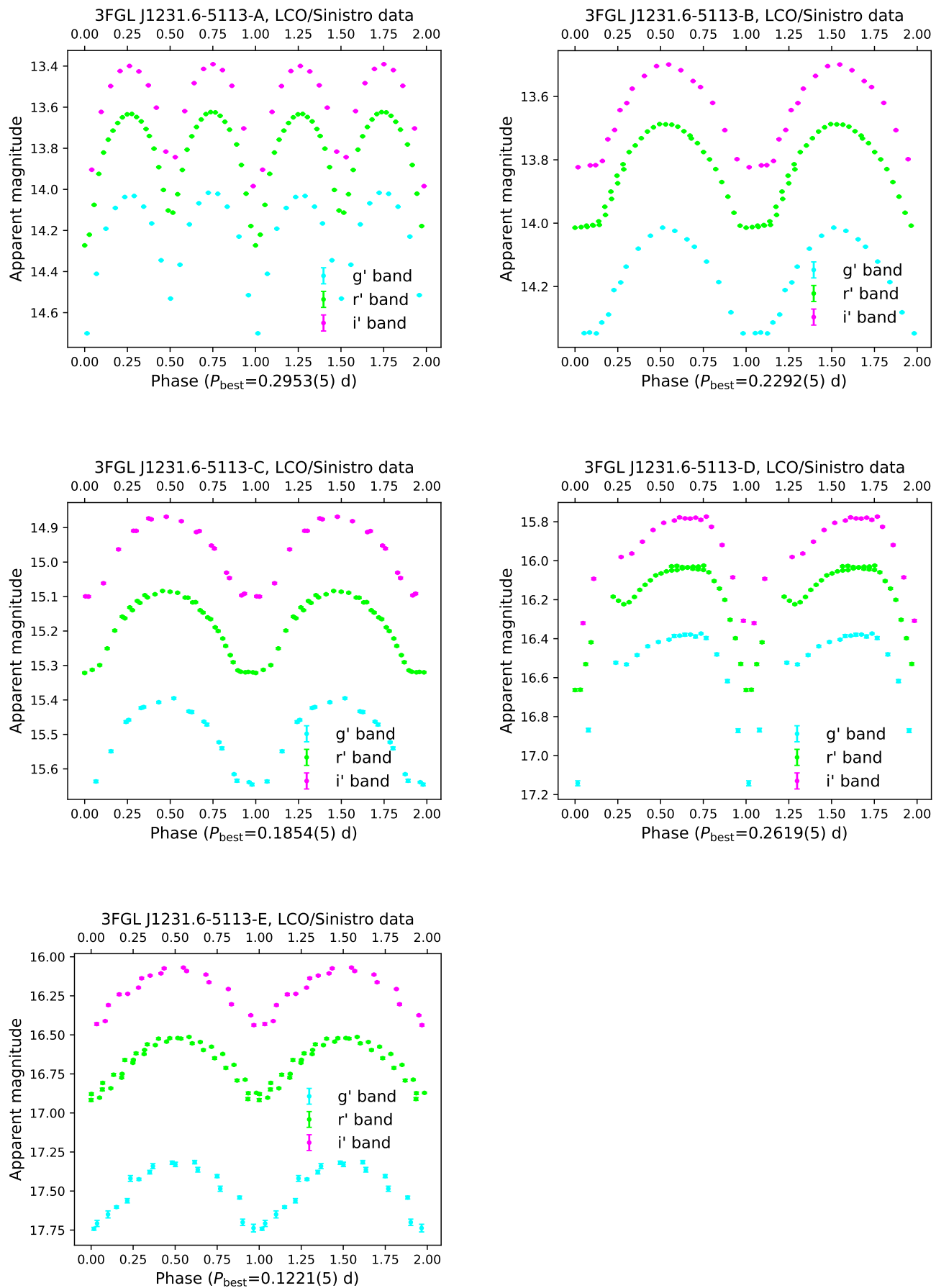


Figure C3. Continued.